University of Central Florida
STARS

Electronic Theses and Dissertations

2014

An Introductory Study of The Dynamics of Autorotation for Wind Energy Harvesting

Bilal Salih
University of Central Florida

 Part of the Mechanical Engineering Commons
Find similar works at: https://stars.library.ucf.edu/etd
University of Central Florida Libraries http://library.ucf.edu

This Masters Thesis (Open Access) is brought to you for free and open access by STARS. It has been accepted for inclusion in Electronic Theses and Dissertations by an authorized administrator of STARS. For more information, please contact STARS@ucf.edu.

STARS Citation
Salih, Bilal, "An Introductory Study of The Dynamics of Autorotation for Wind Energy Harvesting" (2014). *Electronic Theses and Dissertations*. 4518.
https://stars.library.ucf.edu/etd/4518

AN INTRODUCTORY STUDY OF THE DYNAMICS OF AUTOROTATION FOR WIND ENERGY HARVESTING

by

BILAL SALIH
B.S. University of Baghdad, 2009

A thesis submitted in partial fulfilment of the requirements
for the degree of Master of Science
in the Department of Mechanical and Aerospace Engineering
in the College of Engineering and Computer Science
at the University of Central Florida
Orlando, Florida

Spring Term
2014

Major Professor: Tuhin Das

© 2014 Bilal Salih

ABSTRACT

Wind turbines have been used for decades to harvest wind energy. They are suitable only to work on close to ground, and have several drawbacks that are related to the availability of the wind and the amount of extracted power compared with the cost of construction. On the other hand, there is an abundant wind power that is available at high altitudes. The wind jet streams at high elevations $8 - 12\,kms$ are pervasive and persistent, and can potentially produce immense wind energy. Even at moderate elevations of $4 - 5\,kms$, wind power densities are much higher than on ground and more consistent. Consequently, in this thesis research, we investigate the topic of harvesting energy from high altitudes. First, we provide a comprehensive review of two existing theoretical methods that are proposed for airborne wind energy harvesting, the tethered airfoil, and the static autogyro. The latter approach has inherent advantages that warrant further investigation. Autorotation is a well-known phenomenon where a rotor sustains its angular velocity and maintains significant lift in the presence of strong aerodynamic forces and torques generated by interaction with a strong wind field. Autorotation has been researched in the context of free descent of helicopters but has not been considered for energy harvesting. Existing models have mainly focused on statics analysis. In this research, we propose a simple dynamic model of the Autogyro, with the goal of ultimately realizing an Autorotation Energy System (AES). The focus of our work is to provide a preliminary dynamic analysis of autorotation, which is largely absent in current literature, to explore the possibility of using autorotation for designing a multipurpose system that can simultaneously fly at high altitudes and generate energy from the wind. The proposed preliminary dynamic model is used to generate a simulation platform, which is used to explore the autogyros rudimentary maneuvers. Extensive simulation results are provided to evaluate the dynamic performance of AES. Energy harvesting analyses and results are also presented. It is expected that the results will guide the choice of actuations and control that will be necessary for generating combined autorotation and powered

flights that would be net energy generating or energy efficient. The research will be relevant for both tethered and untethered AES and could also be incorporated into multi-rotor based UAVs such as quadrotors.

To my dear father and mother. You are the greatest thing in my life and your love and support will never be forgotten.

To my two angels, Anas and Mary. You keep my spirit alive !

ACKNOWLEDGMENTS

I would like to greatly thank my advisor, Dr. Tuhin K. Das, for his guidance, support, patience, and teaching throughout my education. I deeply appreciate all that he has done for me from the initial developing stages of this thesis. I also would like to thank my committee members Dr. Alain J. Kassab and Dr. Jeffrey L. Kauffman for their valued comments, suggestions, and support.

My deepest gratitude goes to the government of Iraq for providing me with the scholarship and all the needed support to pursue my graduate degree and make this work a reality.

I would like to also acknowledge the help I received from Dr. Zyad Bawatneh whose contribution in editing this thesis is very valuable.

To my family, I could not make it without your support. To my wife, Ruaa Abdulrahman, your endless support and love will never be forgotten. To my best friend, Ghassan Al-Sinbol, I am very grateful for your unconditional help and support To my friends, thank you all for your encouragement and great support. Above all, I give thanks to God for all the good things that I have learned.

TABLE OF CONTENTS

LIST OF FIGURES

LIST OF TABLES

LIST OF ACRONYMS

AES	Autorotation Energy System.
AWE	Airborne Wind Energy System.
BEM	Blade Element Momentum Theory.
C	Autogyro Blade Cord.
c	Mass Center of AES.
C_D, C_L	Drag and Lift Coefficients of the Tethered Airfoil System.
D_a, L_a	Drag and Lift Forces of the Tethered Airfoil System.
D_C, L_C	Drag and Lift Coefficients of the Autogyro.
Er_i	Tethered Airfoil Position Vector.
f	Windmill of AES.
F_a	Actuation Force Applied on the Kite of the Tethered Airfoil .
F_D, F_L	Drag and Lift Forces of the Autogyro.
F_t	Actuation Force Applied on the Base of the Tethered Airfoil .
H	Aerodynamic Longitudinal Force.
H_C	Aerodynamic Longitudinal Coefficient.
HTA	Heavier than Air device.
i	Angle of Incident of the Autogyro.

I_s	Moment of Inertia the shaft of AES.
$\mathcal{L}$	Lagrangian
LTA	Lighter than Air device.
m_{AES}	Mass of AES.
m_E, l_E	Mass and Length of Each Tether Element.
Q	Aerodynamic Torque.
Q_C	Aerodynamic Torque Coefficient .
Q_e	Generator Breaking Torque.
R	Autogyro Blade Radius.
r_c	Position Vector of AES.
S_B	Airfoil System's Base.
S_K	Airfoil System's Kite.
$S_K m$	Mass of the Airfoil.
S_T	Airfoil System's Tether.
$S_T m, S_T l$	Mass and Length of the Airfoil's Tether.
T	Aerodynamic Thrust Force.
T_C	Aerodynamic Thrust Coefficient.
T_S, V_S	kinetic and Potential Energy of the Tethered Airfoil System.
U	Resultant Relative Velocity of the Wind at the Blade Element.

UAV	Unmanned Aerial Vehicle.
$V\prime$	Resultant Velocity Experience by the Autogyro.
Va	Autogyro Velocity.
Va_{rel}	Relative Wind Speed with Respect to the Tethered Airfoil.
V_c	Velocity of AES.
V_W	Wind Speed.
α	Angle of Incident of the Tethered Airfoil System.
γ	Inclination Angle of Relative Wind Speed.
δ	Average Drag Coefficient.
ε	Autogyro Blade pitch Angle.
θ	Inclination angle of the Windmill f with the Horizon.
λ	Tip Speed Ratio.
μ	Axial Flow Ratio.
ϑ	Induced Axial Velocity.
ρ	Air Density.
σ	Blade Solidity.
ϕ	Inclination Angle of the Velocity U .
φ	Angular Position of the Autogyro Blade.
χ	Slop of Blade Element.

ψ	Inclination of the Tether Element.
ψ_K	Inclination of Airfoil's kite with Horizontal.
Ω	Autogyro Angular Velocity about the Rotor Shaft.
ϖ	Flapping Angle.

CHAPTER 1: INTRODUCTION

Renewable energy, produced from infinite resources, has an increasing share of global energy consumption. Wind, which is generated by global climatic phenomena and local weather combination, provides a colossal source of renewable energy. Wind energy has exhibited the most rapid growth among all other renewable energy types [Hod09]. However, it still only contributes a small percentage of the used renewable energy, and needs to be increasingly considered in research and studies. In literature, the most popular machines that are used to convert the kinetic energy available in the wind into electrical power are wind turbines. The wind turbine technology has been used for more than a century to harvest energy only from the wind available near the surface of the earth. Figure 1.1 shows two basic types of wind-turbine configurations: the more common horizontal axis (HAWT), with the gearbox mounted on top of a tower, and the vertical axis (VAWT), with the gearbox at ground level [PM07].

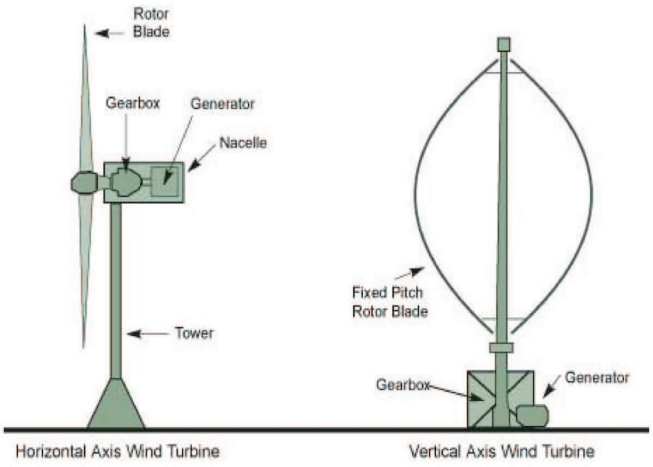

Figure 1.1: Schematic of the Horizontal and Vertical Axis Wind Turbine [PM07]

Wind turbines have been studied extensively. Earlier designs have been continuously developed and refined to improve efficiency. The use of wind turbine technology is geographically restricted and depends on the availability and stability of enough wind velocity at low altitudes. National Renewable Energy Laboratory (NREL) has documented the available wind power near the surface of the earth. In their report [ESH$^+$11], NREL has divided wind speeds magnitude geographically to seven wind power classes (poor to fruitful) as shown in Fig.1.2. The report also provides the annual average wind speeds and the wind power estimates for the United State at altitudes of $10\,m$ and $50\,m$ as seen in Table1.1. These seven classes show a large and significant variability in wind power distribution to the level that class one and two are not appropriate for wind turbines, and only wind power classes of three and above are convenient for wind energy harvesting using ground based turbines. Consequently, the wind turbine technology satisfies a small part of the energy requirements. Add to that, the high cost of construction of wind farms compared with their small power output, it makes wind turbines account only in a small fraction of total generated energy. Therefore, and based on the above-mentioned discussion, it is clear that the abundant wind power near the surface of the earth varies geographically and with altitude. Thus, it is better to harvest wind energy from high altitudes.

Table 1.1: Wind Energy Classes

Wind Power Class	**10m speed (m/s)**	**50m speed (m/s)**
1	4.4	5.6
2	5.1	6.4
3	5.6	7.0
4	6.0	7.5
5	6.4	8.0
6	7.0	8.9
7	9.4	11.9

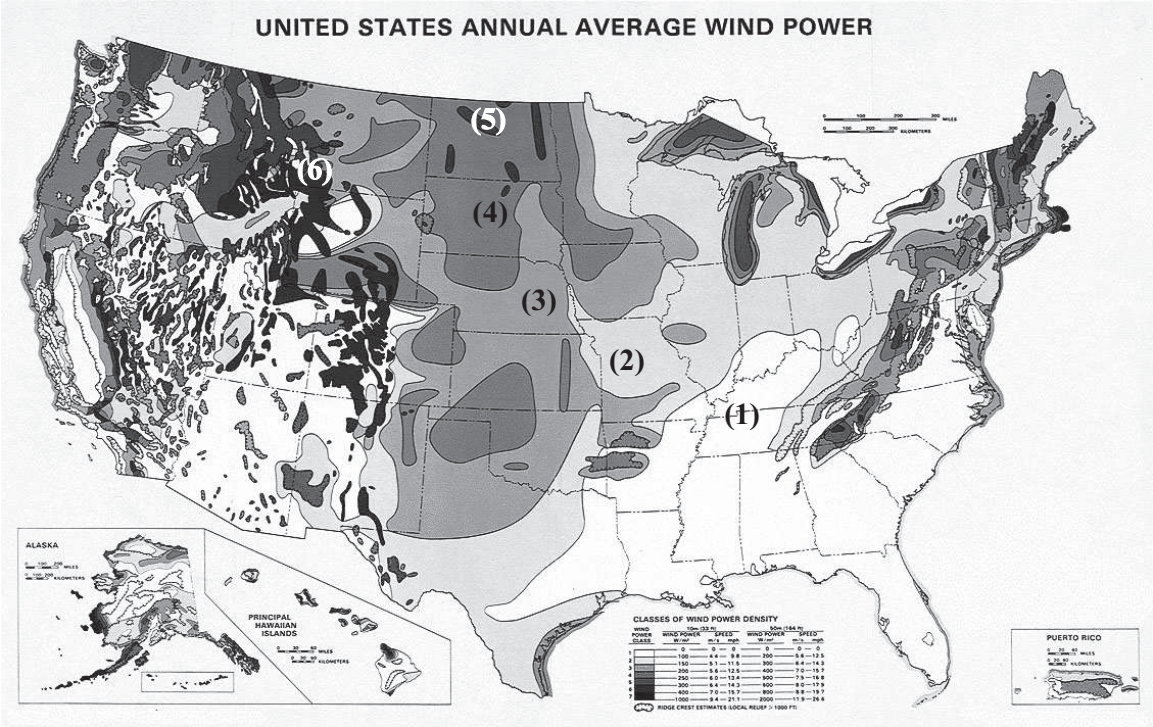

Figure 1.2: Average Annual Surface Wind Energy Distribution Map for USA

1.1 Wind Energy at High Altitude

The data of wind power availability and magnitude at high altitudes presents a totally different picture compared with the wind data from low altitudes. The high altitudes wind data shows that there is an immense and persistent amount of wind power available across the United States; furthermore, the availability of the wind power is not geographically restricted. The first insight into the abundance of the available wind power at altitudes of $7 - 16\,km$ is provided by the study in [AC09], and this abundance of energy at these elevations is attributed mainly to the existence of jet streams high altitudes' global climatic phenomena. The study by [RSC$^+$07] states that high

power densities would be uninteresting if only a small amount of total power was available, and they are estimated to be roughly an order of magnitude higher than (100) times the global energy demand. Furthermore, they are persistent and are typically just a few kilometers away from most energy users; a combination that most energy sources do not possess. In order to quantify wind energy at high altitudes, raw wind speed data downloaded from Integrated Global Radiosonde Archive (IGRA) were analyzed [DVW06]. Three locations that cover a wide range of wind power classes were selected. These locations are: Atlanta (GA) belongs to class one, Buffalo (NY) belongs to class three-four, and Great Falls (MT) belongs to class four-five. The results of the wind power analysis for these three different locations show clearly that there is no significant variation in wind speed, and the average maximum wind speeds of different wind power classes' locations are similar. The results also show that the average wind speeds increase steadily with altitude, up to ($10\,km$).

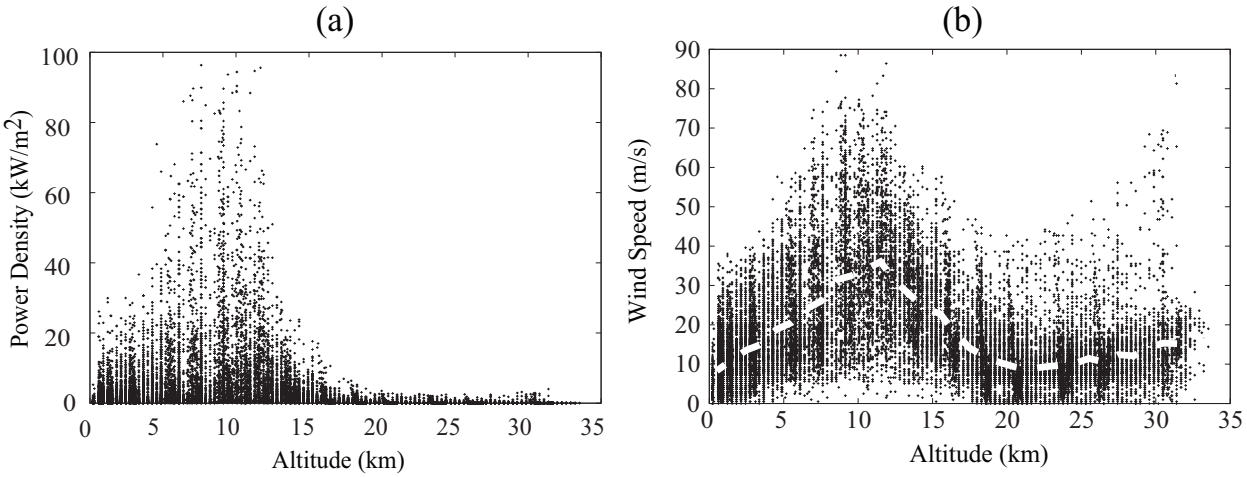

Figure 1.3: Wind Power Density and Annual Wind Speed at High Altitude for Buffalo (NY)

Referring to the aforementioned discussion, and because of the similarities in the wind speed profiles across the three locations, only the variation of wind power density of Buffalo (NY) was investigated. Figure 1.3 shows the data of the wind power density and the annual high altitude wind speed for Buffalo (NY). The wind speed density was evaluated using the relation $P = 0.5\rho V^3$, where ρ is the wind density and V is the wind velocity. Figure 1.4, shows the results of Buffalo (NY)'s analyzed data. The probability distribution of the wind speed above a specific value at different altitudes is plotted in Fig.1.4 (a). Figure 1.4 (b) shows the probability distributions of the wind power densities at altitudes in the range of 1-12 km. The results show that the wind power available at altitudes of $15\,km$ and higher diminishes sharply even though the wind speed at these elevations is significant. This sharp decrease happens because of the atmospheric rarefaction at different altitudes (at 10 km, $\rho \approx 0.41\,kg/m^3$; at the sea level $\approx 1.22\,kg/m^3$). Furthermore, it can be observed from the results that in high altitudes the flow field is persistent and increasingly governed by global phenomena.

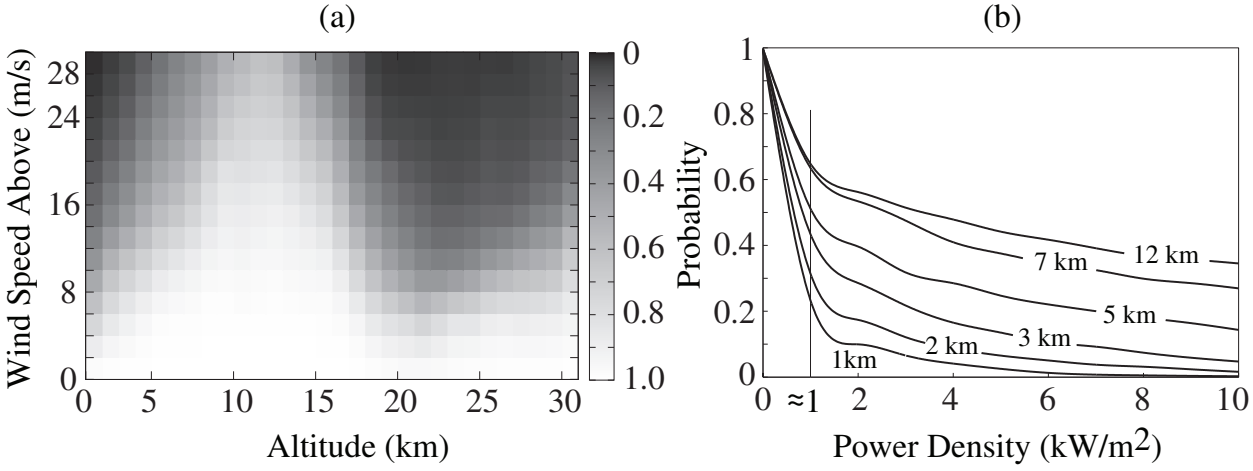

Figure 1.4: High Altitude Wind Power Estimation for Buffalo (NY)

1.2 Airborne Wind Energy Systems

The abundance of available wind energy at high altitudes and the existence of high wind power have increased the interest in Airborne Wind Energy (AWE) devices, and have renewed the attention in their applications. Many reviews of early investigations on airborne wind energy in the form of airborne windmills, and some of the proposed designs can be found in literature. Study in [Man75] has stated that earlier airborne windmills designs were proposed in the first half of (1900s). In these designs, windmills placed on the aircraft were used to generate the power that is needed to run the equipment in communication aerostats. Currently, there are different designs of the AWE system. These designed can be classified according to the system characteristics such as the weight of the system (Lighter than Air (LTA) and Heavier than Air (HTA), and the aerodynamics type (Helicopter, Airfoil, and Aerostat) [GSH12]. Fletcher and B. W Riedler were the first to propose a system in which a tethered rotor-craft is placed permanently in the upper atmosphere to generate electricity and provide the needed lift to support the air-frame [FR79]. Another system that generates power from wind using rotary wings was proposed in [Fle79]. The need of an active control mechanism to maintain a stable flight for such a system was demonstrated by the stability analysis study presented in [Rye85]. In the study [RR84], another idea in which a wind turbine generator is mounted on a tethered aerostat to generate energy was proposed. Many other mechanism systems to generate energy were patented [Kli78] , [Pug84] , [FH78].

In recent years, a renewed interest in AWE has been seen due to the increased interest in alternative energy sources. A kit type AWE designs have been proposed by some researches to harvest energy from low and medium altitudes $< 1\,km$. In the studies by [LW06] and [Ock01], the authors have proposed the Laddermill device which consists of several kites that are connected in series to move a closed cable through a generator. Figure 1.5 shows the original shape of the Laddermil concept.

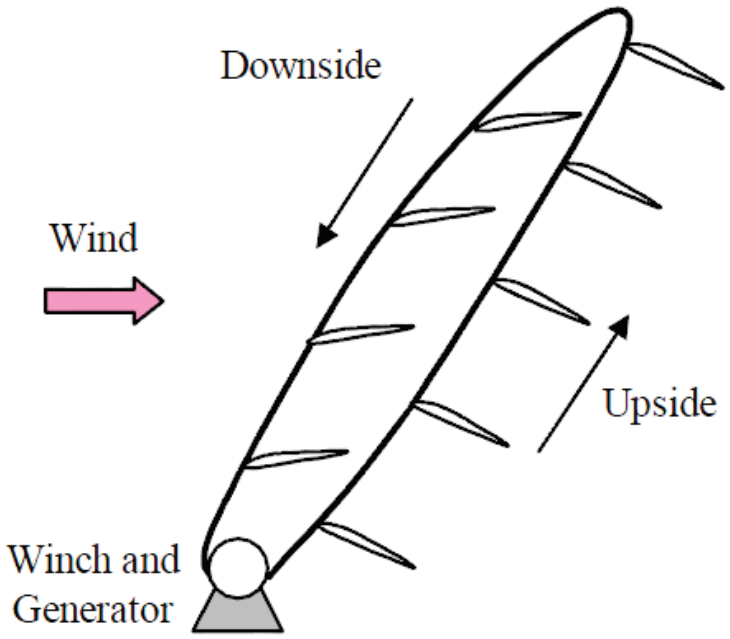

Figure 1.5: The Laddermill Original Design [Ock01]

Several variations were added to the Laddermill devices. The studies in [CFIM06], [CFMI07] proposed a model in which two electrical generators/motors were connected to a kite through two cables. Moreover, the authors in the studies [WLO08a], [WLO07], and [WLO08b] proposed a system of a single kite connected to a cable of varying length, and designed a control model that commands the length of the cable, the kite's roll angle, and the kite's angle of attack to extract energy. Furthermore, studies in [CFM09] and [CFM10] proposed the concept of Kitegen, which is developed later to consist of several kites (kitegen units) that are structured in a circular shape and are installed on the arms of a vertical axis rotor as shown in Fig 1.6 (a). Figure 1.6 (b) shows a schematic of single Kitegen unit.

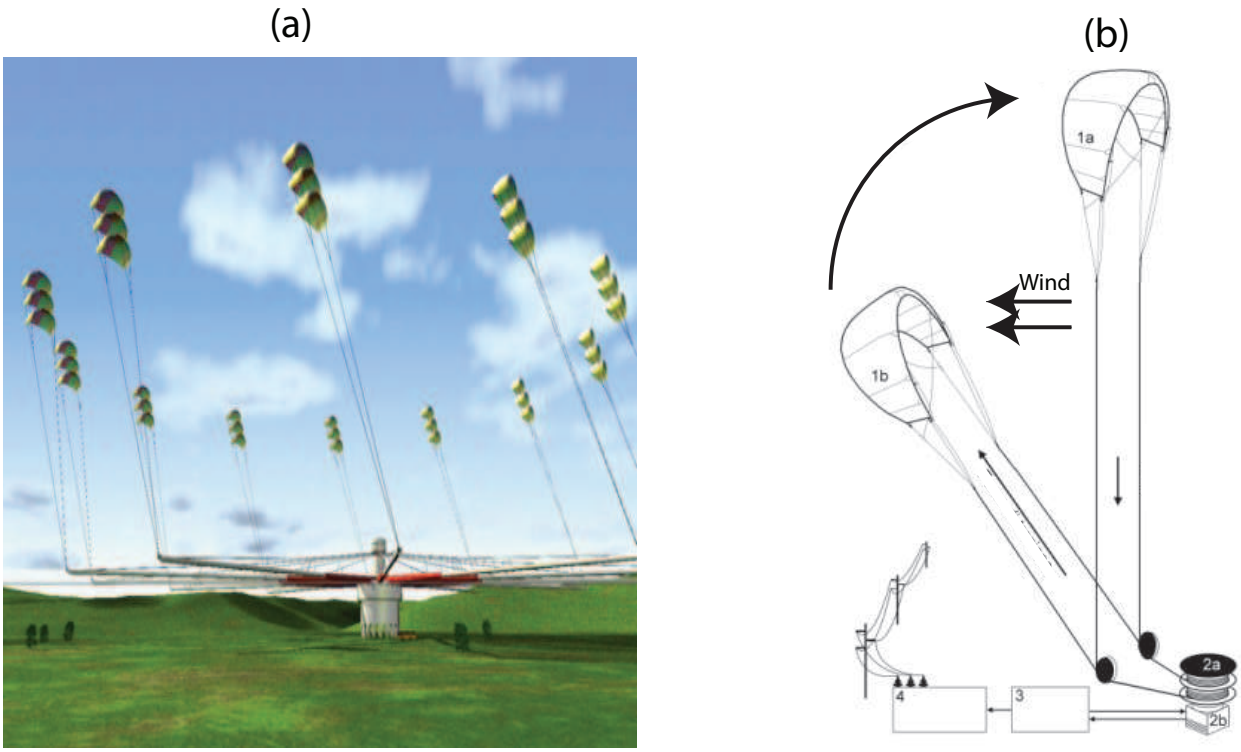

Figure 1.6: The Kitegen Design [CFM10]

It can be observed from these studies that existing AWE designs are predominantly tethered systems and are designed to operate at low altitudes. While tethered AWE systems can be practical for low altitudes, there are challenges in using them for harvesting energy from high altitudes such as the high length tether requirement, the response delay, and the added weight of the tether. On the other hand, high altitude AWE systems should be able to simultaneously generate enough lift, harvest energy from a wind field, flexibly maneuver, and remain enclosed within a bounded region in the atmosphere. Lighter than Air (LTA) systems such as hot air/ helium balloon seem pragmatic and practical for generating simultaneous lift and power. However, they have poor maneuverabil-

ity. Therefore, to utilize the strong wind field at high altitudes for energy harvesting, the design of the AWE systems should have a mechanism that maintains the aforementioned requirements, and makes the system able to simultaneously fly at high altitude and generate energy from the wind. Autorotation phenomenon appears to be a feasible way to provide this multipurpose mechanism, and will be discussed in the next section.

1.3 Autorotation Phenomenon

Autorotation phenomenon is a well-known state of flight in which the aircraft rotor sustains its angular velocity and maintains significant lift in the presence of strong aerodynamic forces and torques generated by interaction with a strong wind field. Autorotation has inherent advantages that warrant further consideration to be investigated for energy harvesting. It can provide the ability to operate at high elevation and produce energy from the wind. During autorotation, the rotor of AWE turns because of the action of the wind field and can be used as a generator to harvest energy. Furthermore, autorotation provides the ability to design $AWEs$ that can switch between two modes of operation, Autorotation and Powered-rotation as needed.

In literature, the principle of autorotation dates to a period of early helicopter development between 1915 and 1920, and refers to the rotors that turn without having an engine, and generate a significant lift due to the aerodynamic torque that is induced by the wind. Traditionally, autorotation has been investigated to build gyrocopters [Cha03], [Phe]. It is also investigated in the context of safe landing of helicopter in the event of engine failure [Lei00]. Autorotation can be fulfilled by using a freely turning rotor placed inclined to a wind field that causes the air to move upward into the rotor and generates an upward thrust. This rotor is termed as an autogyro, and can be considered a generalization of the helicopter. However, in the helicopters, the air is accelerated down into the main rotor system from above direction. Also, autogyros have different actuation structure and an

additional degree of freedom. It consists of three to four blades, each blade can spin freely about the common axis of all the blades. Moreover, each blade can freely rotate (flap) about an axis normal to the spin axis represented by a hinge at its root.

1.4 Motivation and Thesis Contributions

Existing research and development in AWE extraction systems have extensively considered systems that operate at altitudes of ($< 1\,km$), [GSH12]. However, as stated above, persistent jet streams and abundance of wind power densities are available at high altitudes of ($8 - 12\,km$). Therefore, to benefit from the high altitude wind energy, it is essential to extend the operational altitude of AWE systems to the level of ($10\,km$) or even to moderate elevations of ($4 - 5\,km$) at which the wind power densities are much higher than on ground and more consistent. An autogyro-based AWE appears to be a feasible structure on which a pragmatic Autorotation Energy System (AES) can be designed and built to harvest energy from high altitudes. Such a configuration can be potentially used to elevate the Unmanned Aerial Vehicle UAV technology to being more energy efficient. Such $UAVs$ would have prolonged flight time or even be self-sustaining. These $UAVs$ could also offer reduction in cost of communication networks, exploring, surveillance, etc, and serve as a simpler and cheaper alternative to satellites in geographically restricted regions. Moreover, the AES configuration could provide a cost effective means of power generation in remote regions, and enable bulk energy harvesting in a swarm.

In this thesis research, the topic of harvesting energy from strong wind field at high altitudes is investigated. The focus of the work is to explore the possibility and viability of using autorotation principles to design a dynamic system to harvest energy from high altitudes. Autorotation-based systems have not been investigated for wind energy extraction, and their ability of generating lift by rotating freely in the wind field can be utilized in high altitudes to support the weight of the

complete energy extraction system and generate electricity at the same time. The aim of this research is to establish a foundation base and path direction for the wind energy extraction field that can be followed in future investigations and research. Therefore, we propose a simple dynamic model that utilizes the concept of autorotation with the goal of ultimately realizing an Autorotation Energy System (AES). Furthermore, we use the proposed dynamic model to generate a simulation platform to explore the behavior of AES when it is located in a wind field and obtain a preliminary understanding about the autogyro's rudimentary maneuvers.

1.5 Thesis Organization

The remainder of this thesis is organized as follows: In Chapter 2, we present a comprehensive and detailed review of two existing theoretical systems that are proposed for wind energy harvesting, the tethered airfoil and the static autogyro. Chapter 3 describes our proposed dynamic model and provides the mathematical analysis as well as the derivation of the proposed AES. The energy harvesting analysis is also presented in Chapter 3. In chapter 4, we provide the simulation details and approaches. In addition, we present extensive simulation results and discussions about the dynamic performance of AES. Chapter 5 concludes the thesis and discusses our future ideas to extend this work.

CHAPTER 2: WIND ENERGY HARVESTING SYSTEMS

In this chapter, we present a review about the design and analyses of some of the systems that have been proposed for wind energy harvesting. Mainly, two types of systems are presented with the detailed analyses and derivations. The first system design is based on using tethered airfoil, while the second design is based on autorotation theory.

2.1 Tethered Airfoil System for Wind Energy Extraction

Numerous designs of tethered systems have been proposed to be used for wind energy harvesting. In general, these system's designs trend to composite of a number of blades that are attached to a rotating shaft affixed to a rigid standard support. One example of these designs is the Laddermill which is proposed in [LW06] and [Ock01]. Laddermill consists of several kites connected in series by a tether that moves in a continuous and closed loop through a generator with a fixed base. In the study by [CFM10] another system configuration is proposed in which multiple kits are affixed to and controlled by a common base to form a large vertical axis turbine that rotates freely and generates energy. Another system, in which a single kite attached to a movable base by a tethered, is also proposed in [WLO08a]. Moreover, the authors of the study [DM$^+$11] propose another design of a tethered airfoil system for harnessing wind energy. In this study, a two dimensional simple dynamic model is analyzed and simulated. The described system is comprised of an airfoil-like kite mounted by a tether to a grounded base that moves horizontally. The use of a tethered kit and a moving base is quite similar in concept to those aforementioned systems. However, unlike the design proposed by [LW06] and [Ock01], a general moving base is proposed. In addition, the actuation of the kite's inclination is added as an additional degree of freedom compared with the introduced design of [WLO08a]. A schematic of this Tether Airfoil System is shown in Fig.2.1.

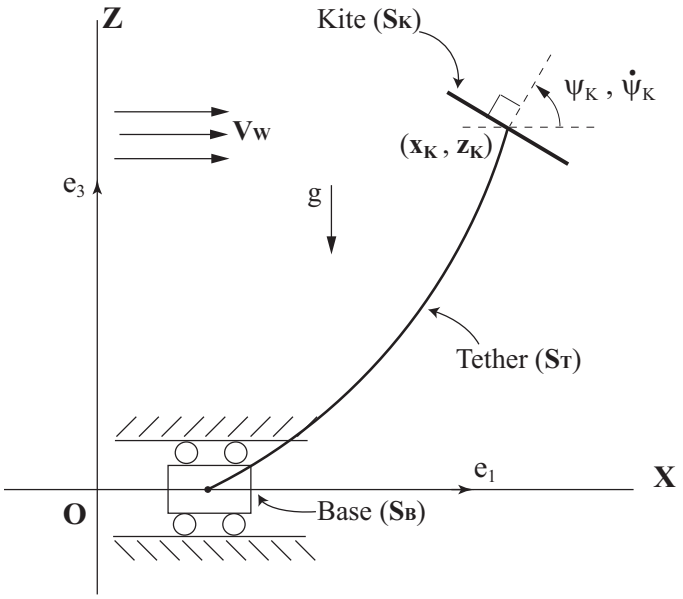

Figure 2.1: Tethered Airfoil System

2.1.1 Dynamic Model and Derivations

In the study by [DM$^+$11], a mathematical model of the tethered airfoil system is derived. In these derivations, the system is assumed to move entirely within the (XZ) plane, and be comprised of an airfoil like kite (S_K), shaped as a flat square plate and connected to a base (S_B) via a tether (S_T) as shown in Fig.2.1 above. It is also assumed that the base (S_B) can move only along the (X) axis, and the inclination of the kite with this axis is controlled by a control system (actuators and sensors) available at the kite. The tether (S_T) is assumed to be unstretched and composed of $(n+1)$ elements (E) connected by mass less rods. The length of each element (l_E) of the tether is assumed to be equal: $(l_E = S_T l/n+1)$, where $(S_T l)$ is the total length of the tether. The mass of each element of the tether (m_E) is defined as: $(m_E = S_T m/n+1)$, where $(S_T m)$ is the total mass of the tether, except the $(n+1)^{th}$ element's mass for which the kite's mass $(S_K m)$ is also considered as the following: $(m_{E_{n+1}} = m_E + S_K m)$. Figure 2.2 shows a tether element (E).

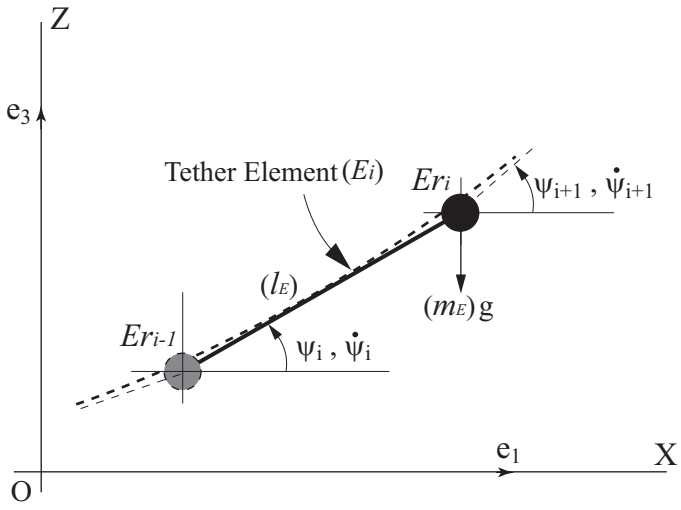

Figure 2.2: A Single Tether Element

2.1.1.1 Dynamic Model

Let $(OXYZ)$ be a fixed frame of references at (O) with the bases $[e_1, e_2, e_3]$, and let (Er_i) be the position vector of each element (E_i) with respect to $(OXYZ)$, where $(i = 1, 2, 3..., n + 1)$. The dynamic model is derived by using Lagrange method as follows:

The position vector of each element (E_i) is:

$$Er_i = X_i\,\hat{e}_1 + Z_i\,\hat{e}_3 \;= [\,x_\circ + \textstyle\sum_{j=1}^{i} l_E\,\cos\psi_j\,]\,\hat{e}_1 \;+\; [\,\sum_{j=1}^{i} l_E\,\sin\psi_j\,]\,\hat{e}_3 \tag{2.1}$$

thus the velocity vector can be obtained by mathematical derivation as:

$$Ev_i \;= \dot{E}r_i \;= [\,\dot{x}_\circ - \textstyle\sum_{j=1}^{i} l_E\,\dot{\psi}_j\,sin\psi_j\,]\,\hat{e}_1 \;+\; [\,\sum_{j=1}^{i} l_E\,\dot{\psi}_j\,\cos\psi_j\,]\,\hat{e}_3 \tag{2.2}$$

By using Lagrange's method, the equations of motion of the system are defined as:

$$\frac{d}{dt}\left(\frac{\partial \mathcal{L}}{\partial \dot{Q}_r}\right) - \frac{\partial \mathcal{L}}{\partial Q_r} = Q\prime_r \tag{2.3}$$

where ($\mathcal{L}$) is the Lagrangian of the system, (Q_r) are the generalized coordinates defining the motion of the system and can be chosen as [ψ_i , $x_\circ$, ψ_k], and ($Q\prime_r$) are the generalized forces and torques of the system. Defining (T_S) and (V_S) as the kinetic and potential energy of the tethered airfoil system respectively, the Lagrangian of the system is evaluated as follows:

The kinetic energy of the system (T_S):

$$T_S = \tfrac{1}{2}\, m_E\, [\, \textstyle\sum_{i=1}^{n} (Ev_i)^2\,] + \tfrac{1}{2}\, m_{En+1}\, \left[(Ev_{n+1})^2\right] + \tfrac{1}{2}\, I\, \dot{\psi}_k^2 \tag{2.4}$$

where the velocities (Ev_i) and (Ev_{n+1}) are obtained from Eq. (2.2).

The potential energy of the system (V_S):

$$\begin{aligned} V_S = &\ [\, m_E\, g \textstyle\sum_{i=1}^{n} Er_i + m_{En+1}\, g\, Er_{n+1}\,] \,.\, \hat{e}_3 \\ = &\ m_E\, g\, [\, \textstyle\sum_{i=1}^{n} \sum_{j=1}^{i} l_E\, \sin\psi_j\,] + m_{En+1}\, g\, [\, \textstyle\sum_{j=1}^{n+1} l_E\, \sin\psi_j\,] \end{aligned} \tag{2.5}$$

where the position vectors (Er_i) and (Er_{n+1}) are obtained from Eq. (2.1).

Therefore, the Lagrangian ($\mathcal{L}$) of the system can be written as:

$$\begin{aligned} \mathcal{L} = &\ T_S - V_S \\ = &\ \tfrac{1}{2}\, m_E\, [\, \textstyle\sum_{i=1}^{n} (Ev_i)^2\,] + \tfrac{1}{2}\, m_{En+1}\, \left[(Ev_{n+1})^2\right] + \tfrac{1}{2}\, I\, \dot{\psi}_k^2 - \\ &\ m_E\, g\, [\, \textstyle\sum_{i=1}^{n} \sum_{j=1}^{i} l_E\, \sin\psi_j\,] - m_{En+1}\, g\, [\, \textstyle\sum_{j=1}^{n+1} l_E\, \sin\psi_j\,] \end{aligned} \tag{2.6}$$

The generalized forces and torques associated with the generalized coordinates are calculated by using the Principle of Virtual Works. The non-conservative forces and torques acting on the system are shown in Fig. 2.3.

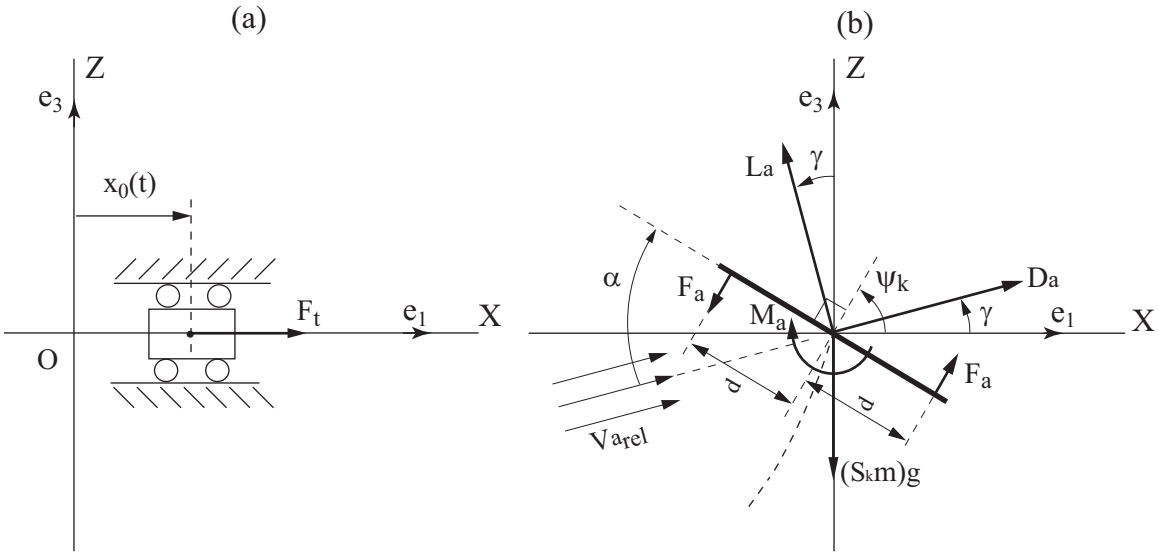

Figure 2.3: Free Body Diagram of (a) the Base and (b) the Airfoil

The virtual work done by the system can be expressed as:

$$\begin{aligned} \delta W = \; & [\,(D_a \cos\gamma - L_a \sin\gamma)\,\hat{e}_1\,]\,.\,[\,\delta x_K\,\hat{e}_1] + [(D_a \sin\gamma + L_a \cos\gamma)\,\hat{e}_3\,]\,.\,[\,\delta z_K\,\hat{e}_3\,] \\ + \; & [\,F_t\,\delta x_\circ\,] + [\,(2F_a d - M_a)\;\delta\psi_k\,] \end{aligned} \tag{2.7}$$

and by using the position vector from Eq. (2.1), the position of the mass center of the kite (S_K) can be written as:

$$x_K = [\,x_\circ + \textstyle\sum_{j=1}^{n+1} l_E\,\cos\psi_j\,], \qquad z_K = [\,\textstyle\sum_{j=1}^{n+1} l_E\,\sin\psi_j\,] \tag{2.8}$$

Therefore the virtual displacement (δx_K) and (δz_K) are expressed as:

$$\delta x_K = [\,\delta x_\circ - \textstyle\sum_{j=1}^{n+1} l_E\, \sin\psi_j\, \delta\psi_i\,], \qquad \delta z_K = [\,\textstyle\sum_{j=1}^{n+1} l_E\, \cos\psi_j\, \delta\psi_i\,] \tag{2.9}$$

By substituting in Eq. (2.7) and carrying out the dot product, the virtual work can be written as:

$$\begin{aligned} \delta W = \;& \textstyle\sum_{j=1}^{n+1} l_E\,[\,(D_a \sin\gamma + L_a \cos\gamma)\cos\psi_j \;-\; (D_a\cos\gamma - L_a\sin\gamma)\sin\psi_j\,]\,\delta\psi_i \\ + \;& [D_a\cos\gamma - L_a\sin\gamma \;+ F_t\;]\delta x_\circ \;+\; [2F_a d - M_a]\,\delta\psi_k \end{aligned} \tag{2.10}$$

Now, by extraction the coefficients of each one of ($\delta\psi_i\,,\ \delta x_\circ\,, \delta\psi_k$), using ($\mathcal{L}$) from Eq. (2.6), with $(Q\prime_{\psi_i} = \delta\psi_i)\,,\ (Q\prime_{x_\circ} = \delta x_\circ)\ and\ (Q\prime_{\psi_k} = \delta\psi_k)$, and substituting them all in Eq. (2.3), we get the following equations:

1. The equation of motion of the generalized coordinates (ψ_i):

$$\begin{aligned} & m_E\, l_E^2\,(n-i+1)\textstyle\sum_{j=1}^{i}\sin(\psi_i-\psi_j)\,\dot\psi_j^2 + m_E\, l_E^2 \sum_{j=i+1}^{n}\Big[\sin(\psi_i-\psi_j)\,\dot\psi_j^2\,(n-j+1)\Big] \\ + \;& m_E\, l_E^2\,(n-i+1)\textstyle\sum_{j=1}^{i}\cos(\psi_i-\psi_j)\,\ddot\psi_j + m_E\, l_E^2 \sum_{j=i+1}^{n}\Big[\cos(\psi_i-\psi_j)\,\ddot\psi_j\, n-j+1)\Big] \\ + \;& (m_E + S_K m)\, l_E^2 \textstyle\sum_{j=1}^{n+1}\cos(\psi_i-\psi_j)\,\ddot\psi_j + (m_E+S_K m)\, l_E^2 \sum_{j=1}^{n+1}\sin(\psi_i-\psi_j)\,\dot\psi_j^2 \\ + \;& m_E\, g\, El\,(n-i+1)\cos\psi_i + (m_E+S_K m)\, g\, l_E\cos\psi_i - l_E\,\sin\psi_i\,\ddot x_\circ\,[m_E\,(n-i+1) \\ + \;& m_E + S_K m] = Q\prime_{\psi_i} = \; l_E\,[\,(D_a\sin\gamma + L_a\cos\gamma)\cos\psi_j \;-\; (D_a\cos\gamma - L_a\sin\gamma)\sin\psi_j\,] \end{aligned} \tag{2.11}$$

2. The equation of motion of the generalized coordinate ($x_\circ$):

$$\begin{aligned} & m_E \textstyle\sum_{i=1}^{n}\ddot x_i + (m_E + S_K m)\;\ddot x_{n+1} + [\,m_E\,(n+1) + S_K m\,]\,\ddot{}x_\circ \\ = \;& Q\prime_{x_\circ} = [\,D_a\cos\gamma - L_a\sin\gamma \;+ F_t\;] \end{aligned} \tag{2.12}$$

3. The equation of motion of the generalized coordinate (ψ_k):

$$I\,\ddot{\psi}_k \;=\; Q\iota_{\psi_k} \;=\; [\,2F_a d - M_a\,] \tag{2.13}$$

2.1.1.2 Lift and Drag Forces

The equations of motion of the tethered airfoil system (2.11), (2.12), and (2.13), derived in the previous section, provide the complete expressions needed to describe the state of motion of the system. In order to solve these equations, the following expression of the aerodynamic force acting on the system, the drag (D_a) and the life (L_a), are defined in similar fashion to those described in [AJ10] :

$$D_a = \tfrac{1}{2}\,C_D\,\rho\,A\,\|\vec{V}a_{rel}\|^2 \tag{2.14}$$

$$L_a = \tfrac{1}{2}\,C_L\,\rho\,A\,\|\vec{V}a_{rel}\|^2 \tag{2.15}$$

The relative wind speed with respect to the airfoil $(\vec{V}a_{rel})$ is defined as the following:

$$\vec{V}a_{rel} = \vec{V_W} - \vec{V_K} = [V_{Wx} - \dot{x}_K]]\,.\,\hat{e}_1 + [V_{Wz} - \dot{z}_K]\,.\,\hat{e}_3 \tag{2.16}$$

substitute the position of the mass center of the kite $(x_K\,,\,z_K)$ from Eq. (2.8) in the relative velocity Eq. (2.16) gives:

$$\|\vec{V}a_{rel}\|^2 = [\,V_{Wx} + \textstyle\sum_{j=1}^{n+1} l_E\,\dot{\psi}_j \sin\psi_j - \dot{x}_\circ\,]^2 + [\,V_{Wz} - \sum_{j=1}^{n+1} l_E\,\dot{\psi}_j \cos\psi_j\,]^2 \tag{2.17}$$

The lift and drag coefficients (C_L) and (C_D) are also defined in similar way to those described in [AJ10]:

$$\frac{dC_L}{d\alpha} = \frac{2\pi}{1 + \frac{2}{e\,AR}}, \quad AR = \frac{b^2}{s} \tag{2.18}$$

$$C_D = c_d + \frac{{C_L}^2}{\pi\, e\, AR} \tag{2.19}$$

where (e) is the span effective factor, (AR) is the aspect ratio with ($b\,,\ s$) as the wing span and wing area respectively, and (c_d) is the profile drag. Subsequently, the formulas of (C_L) for the tethered air foil system are developed as the following: the shape of the wing span is assumed to be square with aside length (a), with one of the corners facing the head wind. The parameter (AR) equals ($2a^2/a^2 = 2$), and (e) is obtained from experimental values and taken as (0.8), see [AJ11]. Substitute these values in Eq. (2.18), (C_L) is obtained as follows:

$$\begin{aligned} \frac{dC_L}{d\alpha} = \frac{2\pi}{1 + \frac{2}{(0.8)\,(2)}} &\Rightarrow dC_L(1 + 1.25) = 2\,\pi\,d\alpha \\ &\Rightarrow C_L = \int 2.793\,d\alpha = 2.793\,\alpha + Cons \end{aligned} \tag{2.20}$$

Now, to calculate the value of the $Cons$, the angle of attack for a zero lift ($\alpha_{L,0}$) is selected based on experimental data and chosen to be equal (-0.035 rad $\approx -2^\circ$) as presented in [AJ11], [AJ10]. Using the expression of (C_L) from Eq. (2.20):

$$C_L = 0 = 2.793\,\alpha_{L,0} + Cons \Rightarrow Cons = 4.793 \tag{2.21}$$

thus the final expression for (C_L) is:

$$C_L = 2.793(\,\alpha + 0.035) \tag{2.22}$$

The drag profile (c_d) is defined similarly to the one in [Whi09] and given as:

$$c_d = 0.1943\,\alpha^2 + 0.00625 \tag{2.23}$$

Using the expressions of (C_L), (C_D), and (c_d) from Eqs. (2.19), (2.22) and (2.23) respectively, the drag coefficient (C_D) can be developed as:

$$\begin{aligned} C_D = &\quad 0.1943\,\alpha^2 + 0.00625 + \frac{C_L^2}{5.0265} \\ = &\quad 0.1943\,\alpha^2 + 0.199\,C_L^2 + 0.00625 \end{aligned} \tag{2.24}$$

2.1.2 Energy Extraction Analysis

The discussed tethered airfoil system is used to investigate the extraction of wind energy through the base actuation. For this purpose, a simulation is constructed to demonstrate the feasibility of energy harvesting. In this simulation, the wind speed is assumed to have a time steady magnitude and direction with a value of ($17\,m/s$) for the horizontal component (V_{Wx}) and ($Zero\ m/s$) for the vertical component (V_{Wz}). The values of other parameters involved in the calculations are defined as shown in the Table 2.1. The initial conditions are defined as $(\psi_i(0) = 0.5)$ rad and $(\dot{\psi}_i(0) = 0\,rad/s)$ for $(i = 1, 2, \cdots, 10)$. The base motion actuation signal is assumed to be a sinusoidal with an amplitude of ($6\,m$) and a frequency of ($0.2\,Hz$). Additionally, the angle (ψ_k) is assumed to vary in synchronization with the base motion, with amplitude and frequency equal ($6.5°$) and ($0.2\,Hz$) respectively, and is shifted by ($110°$).

Table 2.1: Tethered System Simulation Parameters

Parameter	**Value**
$n+1$	10
A	25 m^2
d	0.5 m
I	2.5 Kgm^2
$S_K m$	3 Kg
$S_T l$	100 m
$S_T m$	0.5 Kg
ρ	1.3 Kgm^{-3}

During the simulation, the system is also allowed first to converge to equilibrium from $(t = 0)$ to $(t = 150)$ with equilibrium values ($\alpha = 90 - \psi_k$, $\gamma = 0$), and then the actuation is initiated. Consequently, $(x_\circ(t))$ and (ψ_k) are identified as:

$$x_\circ(t) = \begin{cases} 0 & \text{for} \quad t < 150 \text{ s} \\ 6\sin\left(0.4\pi(t-150)\right) & \text{for} \quad t \geq 150 \text{ s} \end{cases} \tag{2.25}$$

$$\psi_k = \begin{cases} 75^\circ & \text{for} \quad t < 150 \text{ s} \\ 81.11^\circ - 6.5^\circ \sin\left(0.4\pi(t-150) + 110^\circ\right) & \text{for} \quad t \geq 150 \text{ s} \end{cases} \tag{2.26}$$

The actuation of the base coupled with the variation of the angle of inclination cause the kite to move periodically in a close path as shown in Fig. 2.4. As a result, the base moves horizontally in a back and forth motion with a distance of $(x_\circ(t))$. The base's periodic motion derives a generator, attached to the base, with the force (F_t) and causes it to turn and produce energy continuously.

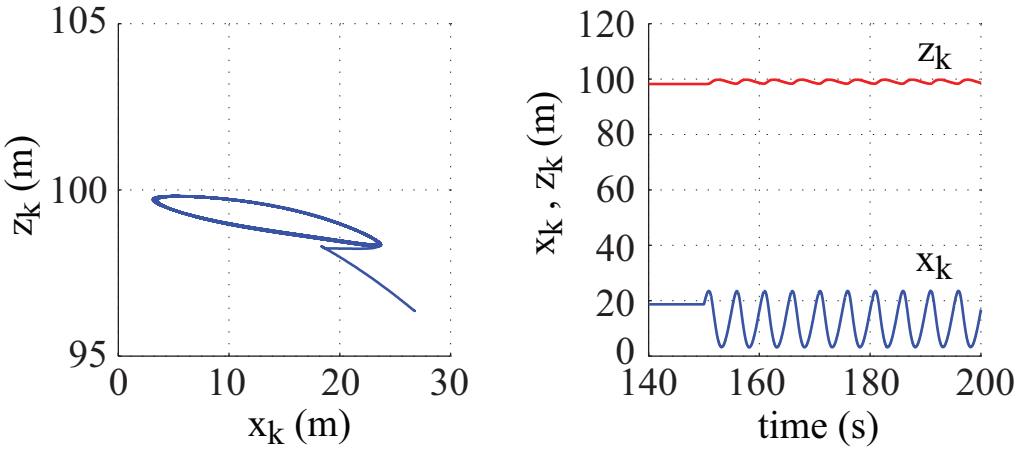

Figure 2.4: Motion of the Airfoil

The amount of the extracted energy is obtained and plotted in Fig. 2.5 based on the force (F_t) by using the following integral:

$$E_{ext} = \int_0^t F_t \, \dot{x}_\circ \, dt \tag{2.27}$$

In this simulation, the assumed high value of the wind speed leads to produce a large magnitude of (F_t), and generate a power that equals approximately to $(120000J/150s = 800\,watt)$ as seen from Fig. 2.5.

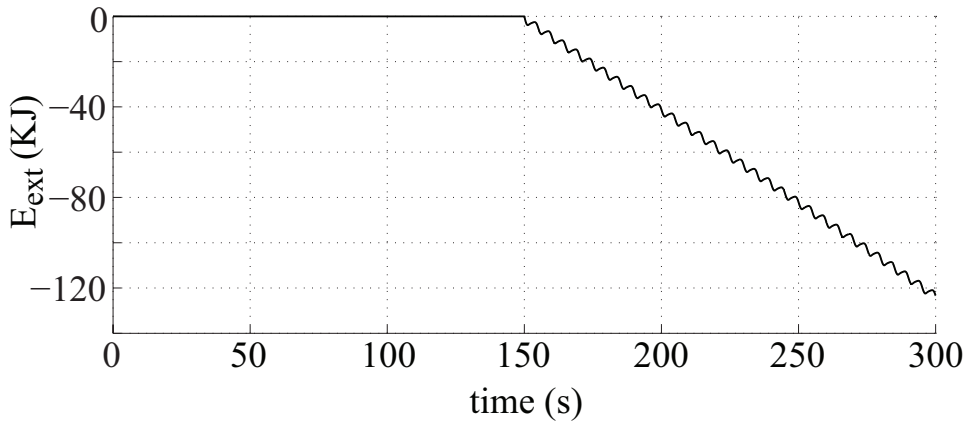

Figure 2.5: Tethered System Wind Energy Extraction Results

2.2 Autogyro System for Wind Energy Extraction - *Static Analysis*

Autorotation has not been sufficiently investigated for wind energy harvesting. In a study done by [RSC$^+$07], a power generator using autorotation principle is discussed without providing mathematical analysis. A preliminary study about using autogyro for harvesting energy from high altitude has been carried out by the study in [RD13]. A mathematical model, using the first principle of the autogyro, has been developed based on autorotation theory presented in the study by [Gla26]. The mathematical analysis are developed under some assumptions and through several steps. The expressions of aerodynamic forces and torques, the thrust force, the longitudinal force, and the rotor torque that arise from the rotating blades, are derived for a rotor inclined at an angle of incident, and translating with a speed in still air.

2.2.1 Mathematical Model and Derivations

The model, used in the derivations analysis presented in [Gla26], is comprised of a single rotor whose plane of rotation is inclined backwards at angle (i) with the horizon, and attached to a large radius (R) windmill. The wind mill consists of four identical blades, whose cord length (c) is constant from root to tip, and are attached to the rotor shaft at small positive angle of pitch (ε). The model is assumed to be subjected to a wind field with a speed of (V_w) that provides the rotation of the windmill with an angular velocity of (Ω), and generates the aerodynamic forces and torques, the thrust force (T) along the shaft, the longitudinal force (H) at right angle to the thrust force (T) in in the plane of the shaft in the direction of motion, and the rotor torque (Q) about the shaft. The resultant aerodynamic forces acting on the autogyro can be also expressed as a drag force (F_D) along the direction of the wind, and a lift force (F_L) in a direction normal to it. Figure 2.6 shows a schematic picture of the autogyro model with all the associated forces.

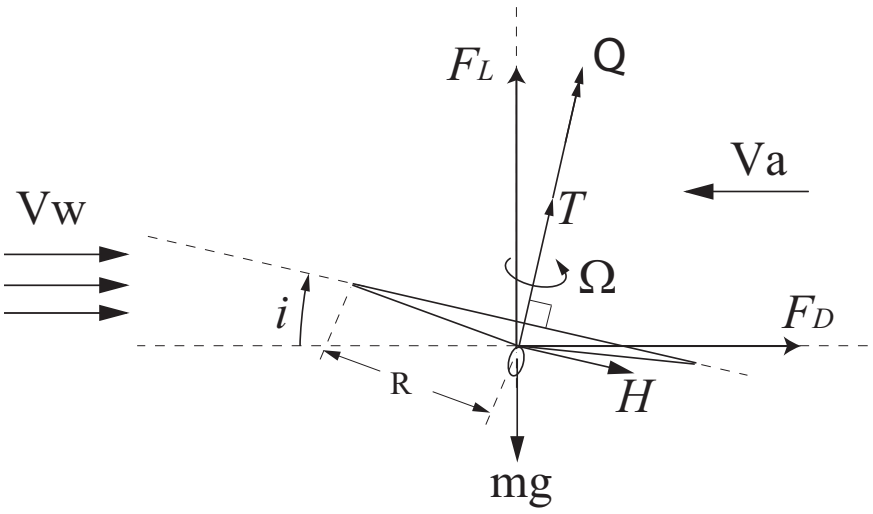

Figure 2.6: Forces Acting on an Autogyro

2.2.1.1 Motion of the Blades

The instantaneous position of the windmills blades is defined using two different angles. The first angle is the angular position of the blade (φ) through which the blade is spinning about the rotor shaft in the same direction of the wind. The second one is the flapping angle (ϖ) which represents the angular rotation of the blade about a hinge at its root in upward direction above the plane normal to the rotor shaft. The angle (ϖ) is assumed to be a periodic function of the angle (φ), and can be expressed using Fourier series form as the following:

$$\varpi = \varpi_0 - \varpi_1 \cos(\varphi - \varphi_1) - \varpi_2 \cos 2(\varphi - \varphi_2) - \cdots \tag{2.28}$$

where (ϖ_0), (ϖ_1), (ϖ_2), (φ_1), (φ_2), etc, are assumed to be the positive parameters of the Fourier series form of the flapping motion in such a way that (ϖ_1) is the upward inclination angle of the blade associated with the angular position of blade (φ_1), and so on. Providing the assumption that

the angle (ϖ) is small, it is sufficient to consider only the main flapping oscillation by neglecting all the higher harmonics including ($\cos 2\varphi$, etc) and retaining only the first harmonic term as in Eq.(2.29). Figure 2.7 shows a three blades rotor with the angles (φ) and (ϖ).

$$\varpi = \varpi_0 - \varpi_1 \cos(\varphi - \varphi_1) \tag{2.29}$$

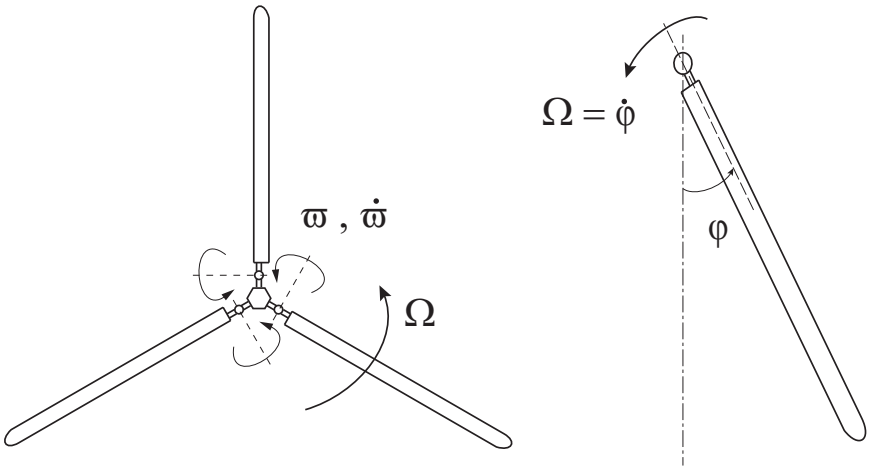

Figure 2.7: Blades Rotation Angles

2.2.1.2 Interference Flow and Induced Velocity

The induced velocity of the system is evaluated based on the nature of the autogyros velocity (V_a). The autogyro whose windmill is inclined at angle (i) has two velocity components: the axial velocity ($V_a \sin i$) and the sideslip velocity ($V_a \cos i$). The effect of those two components is not equal, and the sideslip velocity is considerably larger than the axial velocity. This inequality leads to consider only the induced axial velocity (ϑ) which assumed to be constant over the entire span (R) in a direction parallel to the shaft of the autogyro, and expressed using the form of the induced

velocity of the airfoil with semi span (R) and lift (T) as the following:

$$\vartheta = \frac{T}{(2\pi\, R^2\, \rho\, V\prime)} \tag{2.30}$$

where ($V\prime$) is the resultant velocity experienced by the autogyro and expressed in the following form:

$$V\prime = ((V_a\, \sin i - \vartheta\,)^2 + {V_a}^2 \cos^2 i)^{1/2} \tag{2.31}$$

2.2.1.3 Aerodynamic Forces

Considering the aerodynamics principals of a rotating system, the aerodynamic forces can be expressed in the form of non-dimensional coefficients. By using the disk area of the windmill ($\pi\, R^2$) and the tip speed ($\Omega\, R$) as a fundamental area and speed respectively, ($T,\ H,\ and\, Q\,$) can be defined as follows:

$$T = T_c\, \pi\, R^2\, \rho\, \Omega^2\, R^2 \tag{2.32}$$

$$H = H_c\, \pi\, R^2\, \rho\, \Omega^2\, R^2 \tag{2.33}$$

$$Q = Q_c\, \pi\, R^2\, \rho\, \Omega^2\, R^2\, R \tag{2.34}$$

where (T_c) is the thrust force coefficient, (H_c) is the longitudinal force coefficient, and (Q_c) is the torque coefficient. The drag (F_D), and lift (F_L) can be also defined using the forward speed of the autogyro (V_a) as a fundamental speed and (D_C, L_C) as drag and lift coefficients respectively as shown in the following equations:

$$F_D = \tfrac{1}{2}\, D_C\, \pi\, R^2\, \rho\, {V_a}^2 \tag{2.35}$$

$$F_L = \tfrac{1}{2}\, L_C\, \pi\, R^2\, \rho\, {V_a}^2 \tag{2.36}$$

2.2.1.4 Aerodynamic Coefficients

The coefficients of the aerodynamic forces and torques acting on the autogyro are derived using the Blade Element Momentum theory approach (BEM) introduced in [GM52], which is basically an application of the standard process of airfoil theory to rotating blades [SN01]. In these derivations, the resultant forces and torques are first derived for a blade element (dr) chosen at one of the windmills blades that rotate with an angular position (φ), then this blade element is integrated over each blade span. The blade element is located at a redial distance (r) along the blade, and inclined at a small angle ($\varpi + \chi$), where (ϖ) is the blade's flapping angle, and (χ) is a geometric property due to the curvature of the blade (the slop of the blade element). The velocity of the wind relative to the motion of the chosen blade element is calculated based on the velocity of the wind (V_w), and the angular velocity of the blade (Ω). Therefore, the resultant relative velocity of the wind (U) at

the blade element, inclined at angle (ϕ), has the following components:

$$\begin{aligned} U_r &= u\,(\varpi\ +\ \chi) + V_w \cos i\ \cos\varphi \\ U_T &= U\cos\phi = \Omega r + V_w \cos i\ \sin\varphi \\ U_P &= U\sin\phi = u - r\dot{\varpi} - (\varpi\ +\ \chi)\,V_w\ \cos i \cos\varphi \end{aligned} \tag{2.37}$$

where ($V_w\ \cos i$) is the normal component of the autogyro velocity, and (u) is the axial velocity along the shaft and can be expressed conveniently as:

$$u = (\,V_w \sin i\ -\ \vartheta) = \mu\,\Omega\,R \tag{2.38}$$

where (μ) is the axial flow ratio ($\frac{u}{\Omega\,R}$). Figure 2.8 shows the velocity's components of the blade element.

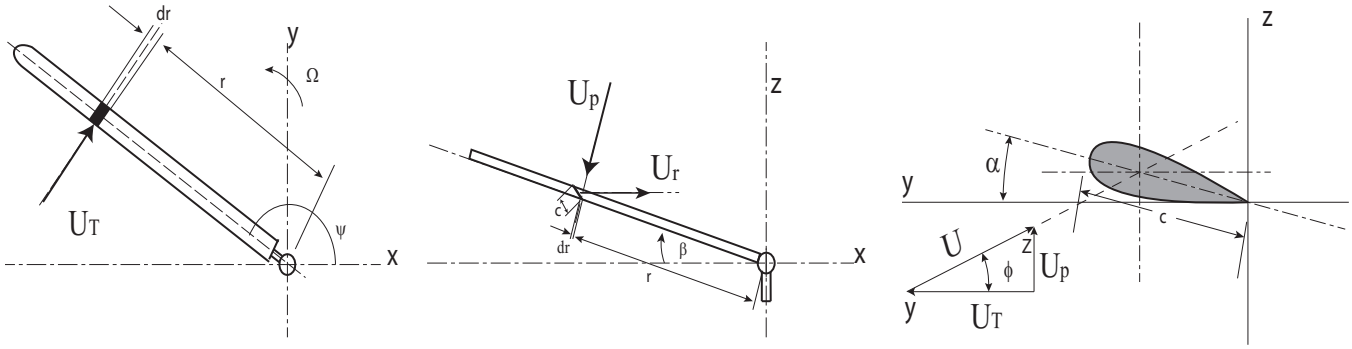

Figure 2.8: Velocity Components of a Blade Element

Assuming that the radial velocity component is negligible ($U_r \approx 0$), the angle (ϖ) and (ϕ) are small, and ($\dot{\varpi} = d\varpi/dt = \varpi_1 \sin(\varphi - \varphi_1)\ \dot{\varphi},\ \dot{\varphi} = \Omega$) and ($u$) is from Eq.(2.38), the net resultant relative velocity of the wind at the blade element becomes:

$$\begin{aligned} U^2 &= U_p^2 + U_T^2 \\ U_T &= \Omega r + V_w \cos i \sin\varphi \\ U_p &= \mu\Omega R - \Omega r \varphi_1 \sin(\varphi - \varphi_1) - (\varphi_0 + \chi) V_w \cos(i) \cos\varphi \end{aligned} \tag{2.39}$$

Using the velocity (U) and the area of the element ($c\,dr$), the drag and lift forces acting on the blade element can be expressed as:

$$dF_D = \tfrac{1}{2}\, d_C\, \rho\, U^2 c\, dr \tag{2.40}$$

$$dF_L = \tfrac{1}{2}\, l_C\, \rho\, U^2 c\, dr \tag{2.41}$$

The blade's lift coefficient (l_C) is assumed to be proportional to the angle of incident of the blade element which represents the summation of the angle of pitch (ε) and the angle (ϕ). Thus, (l_C) equals to:

$$l_C = K\,(\varepsilon + \phi) \tag{2.42}$$

The contribution of the drag coefficient (d_C) in the forces components is assumed to be small compared with the lift coefficient contribution, and therefore, it can be replaced by a small value (δ) which represents the average drag coefficient.

The expressions of the steady state ($T,\ H,\ and\, Q$) forces acting on the blade element can be defined in terms of element's drag and lift forces as follows, see Fig 2.9:

$$dT = dF_L \cos\phi + dF_D \sin\phi \tag{2.43}$$

$$dQ = dF_q r = (dF_L \sin\phi - dF_L \cos\phi) r \tag{2.44}$$

$$\begin{aligned} dH &= \tfrac{dQ}{r} \sin\varphi + dT \sin(\varpi + \chi) \cos(180 - \varphi) \\ &= \tfrac{dQ}{r} \sin\varphi - dT \sin(\varpi + \chi) \cos\varphi \end{aligned} \tag{2.45}$$

By utilizing Eqs. (2.43), (2.44), and (2.45), with the assumption that the angles (ϕ) and ($\varpi + \chi$) are all small, the following approximations can be made: ($\cos\phi = 1,\ \sin\phi = \phi,\ sin(\varpi + \chi) = (\varpi + \chi),\ dT = Dl$). Therefore, the force's coefficients can be calculated as below:

<u>1- Thrust</u>:

Using Eq. (2.42) with $(K = 3)$ and Eqs. (2.41) and (2.43), the thrust force for a one blade of the autogyro can be expressed as:

$$\begin{aligned} dT_1 &= \tfrac{1}{2}\, l_C\, \rho\, U^2 c\, dr = \tfrac{3}{2}\, \rho\, c\, (\varepsilon + \phi) U^2\, dr \\ \Rightarrow T_1 &= \int_0^R \tfrac{3}{2}\, \rho\, c\, (\varepsilon + \phi) U^2\, dr \end{aligned} \tag{2.46}$$

Therefore, the total thrust force for (B) blades of a constant cord, along the span can computed as:

$$T = \tfrac{B}{2\pi} \int_0^{2\pi} d\varphi \int_0^R \tfrac{3}{2}\, \rho\, c\, (\varepsilon + \phi) U^2\, dr \tag{2.47}$$

and by evaluating the above integration, the total thrust (T) is:

$$T = B\,c\,\rho\Omega^2\,R^3\left(\varepsilon + \tfrac{3}{2}\mu\right) \tag{2.48}$$

Introducing the blade solidity ($\sigma = B\,c/\pi\,R$) to represent the ratio of the blade to the disk area, and subtracting the Eq. (2.48) from the expression of (T) in Eq. (2.32), the thrust coefficient can be represented as:

$$T_c = \sigma\left(\varepsilon + \tfrac{3}{2}\mu\right) \tag{2.49}$$

2- Torque:

Using the Eq. (2.42) with $(K = 3)$ and ($d_C = \delta$), and the Eqs. (2.40), (2.41), and (2.44), the torque for a one blade of the autogyro can be expressed as:

$$\begin{aligned} dQ_1 = &\ \tfrac{1}{2}\,(l_C\phi - d_C)\,r\,\rho\,U^2 c\,dr = \tfrac{1}{2}\,\rho\,c\,(-3\varepsilon\phi - \phi^2 + \delta)U^2\,dr \\ \Rightarrow Q_1 = &\ \int_0^R \tfrac{1}{2}\,\rho\,c\,(3\varepsilon\phi + 3\phi^2 - \delta)U^2\,dr \end{aligned} \tag{2.50}$$

then, the total torque for (B) blades of a constant cord, along the span can computed as:

$$Q = \tfrac{B}{2\pi}\int_0^{2\pi} d\varphi \int_0^R \tfrac{1}{2}\,\rho\,c\,(3\varepsilon\phi 3\phi^2 - \delta)U^2\,dr \tag{2.51}$$

by evaluating the above integration, the average aerodynamic torque generated over one complete rotation, Torque (Q) is:

$$Q = B\,c\,\rho\Omega^2\,R^4\tfrac{1}{4}\,(6\mu^2 + 4\varepsilon\mu - \delta) \tag{2.52}$$

Similarly, using ($\sigma = B\,c/\pi\,R$), and subtracting the Eq. (2.52) from the expression of (Q) in Eq, the torque coefficient can be represented as:

$$Q_c = \tfrac{\sigma}{4}\,(6\mu^2 + 4\varepsilon\mu - \delta) \tag{2.53}$$

Another expression of (Q_c) in term of (T_c) from Eq. (2.49) can be also written as:

$$Q_c = \sigma\mu\left(\tfrac{3}{2}\mu + \varepsilon\right) - \tfrac{\delta\,\sigma}{4} = \mu T_c - \tfrac{\delta\,\sigma}{4} \tag{2.54}$$

3- Longitudinal force:

The Longitudinal force of the autogyro can be expressed using Eq. (2.45) as the following:

$$dH = \tfrac{dQ}{r}\sin\varphi - dT(\varpi\ +\ \chi)\cos\varphi \tag{2.55}$$

where the expressions for (dT) and (dQ) can be obtained from Eqs. (2.46), (2.50). Then for a one blade, the longitudinal force can be expressed as:

$$\begin{aligned} dH_1 =&\ \ [\tfrac{1}{2}\,\rho\,c\,(-3\varepsilon\phi - \phi^2 + \delta)U^2\,dr]\sin\varphi - [\tfrac{3}{2}\,\rho\,c\,(\varepsilon+\phi)U^2\,dr](\varpi\ +\ \chi)\cos\varphi \\ \Rightarrow H_1 =&\ \ \textstyle\int_0^R \tfrac{1}{2}\,\rho\,c\,[\frac{1}{r}(-3\varepsilon\phi - 3\phi^2 + \delta)\sin\varphi - 3(\varepsilon+\phi)(\varpi\ +\ \chi)\cos\varphi]U^2\,dr \end{aligned} \tag{2.56}$$

and the total Longitudinal force (H) for (B) blades of a constant cord, along the span can computed as:

$$H = \tfrac{B}{2\pi}\textstyle\int_0^{2\pi} d\varphi \int_0^R \tfrac{1}{2}\,\rho\,c\,[\frac{1}{r}(-3\varepsilon\phi - 3\phi^2 + \delta)\sin\varphi - 3(\varepsilon+\phi)(\varpi\ +\ \chi)\cos\varphi]U^2\,dr d\varphi \tag{2.57}$$

By evaluating the above integration, the total longitudinal force (H) is:

$$H = B\,c\,\rho\Omega^2\,R^3\left[\tfrac{1}{2}\delta + \tfrac{8}{3}\varepsilon^2 + \tfrac{13}{2}\varepsilon\mu + \tfrac{9}{2}\mu^2 + \tfrac{1}{12}\varpi_0^2 + (8\eta_2 - 3\eta_1\varpi_0) - 24\eta_2^2 + \tfrac{1}{2}\xi\right]\frac{V_w\cos i}{\Omega R} \tag{2.58}$$

comparing with the expiration of (H) from Eq. (2.33) and using (σ), the Longitudinal coefficient can be represented as:

$$H_c = \sigma\left[\tfrac{1}{2}\delta + \tfrac{8}{3}\varepsilon^2 + \tfrac{13}{2}\varepsilon\mu + \tfrac{9}{2}\mu^2 + \tfrac{1}{12}\varpi_0^2 + (8\eta_2 - 3\eta_1\varpi_0 - 24\eta_2^2 + \tfrac{1}{2}\xi\right]\frac{V_w\cos i}{\Omega R} \tag{2.59}$$

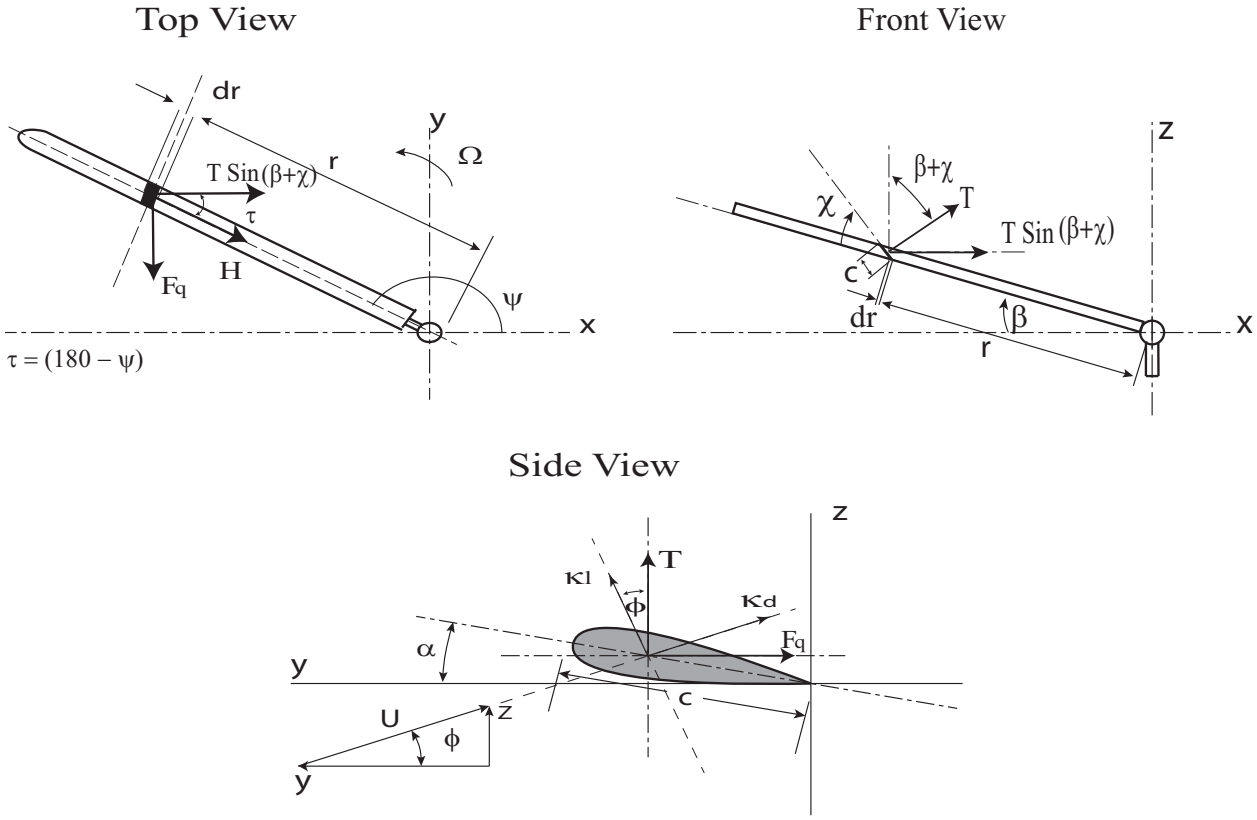

Figure 2.9: Blade Element Forces

2.2.1.5 Angular Velocity and Axial Flow Ratio Calculations

The above-mentioned derivations provide the needed expressions to calculate the aerodynamic forces ($T,\ H,\ and\, Q$). However, to be able to solve the equations, the expressions for the axial flow ration (μ) and the angular velocity (Ω) need to be derived first. The steady state expression of the axial flow ratio is determined using the assumption that, under the steady state operation, the aerodynamic torque (Q) must be $zero$. Using the Eq. (2.52) with ($Q = 0$), we can have the following:

$$\begin{aligned} Q = &\quad B\, c\, \rho \Omega^2\, R^4 \tfrac{1}{4}\, (6\mu^2 + 4\varepsilon\mu - \delta) = 0 \\ \Rightarrow &\quad \tfrac{1}{4}\, (6\mu^2 + 4\varepsilon\mu - \delta) = 0 \end{aligned} \tag{2.60}$$

By solving Eq. (2.60), considering that a sensible solution required (μ) to be a positive value, the parameter (μ) in terms of the angle of pitch (ε) and the drag coefficient (δ) is defined as:

$$\mu = \tfrac{1}{3} \left[\sqrt{\varepsilon^2 + \tfrac{3}{2}\delta} - \varepsilon \right] \tag{2.61}$$

The equation of the thrust force (T) is used to derive the expression of the angular velocity (Ω). In this derivation, the autogyro is assumed to provide a thrust force ($T = Wd$), where ($Wd > W$) and (W) being the total weight of the autogyro to be supported. Using Eqs. (2.32) and (2.49) with ($T = Wd$), we can have the following expression:

$$T = \sigma \left(\varepsilon + \tfrac{3}{2}\mu \right)\, \pi\, R^4\, \rho\, \Omega^2 = Wd \tag{2.62}$$

Therefore, the angular velocity of the system (Ω) in any particular case can be given as:

$$\Omega = \sqrt{\frac{W_d}{\sigma\left(\varepsilon + \frac{3}{2}\mu\right)\,\pi\,R^4\,\rho}} \tag{2.63}$$

2.2.2 Energy Extraction Analysis

The discussed autogyro model with the derived steady state equations is used to explore the energy harvesting possibility. For this investigation, the velocity (V_w) is assumed to be the steady state horizontal wind speed instead of the steady aircraft speed in still air. Furthermore, an electrical generator, assumed to be attached to the autogyro rotor, is used to extract the wind energy. During energy extraction, the generator reduces the steady state angular velocity (Ω) by providing a load torque (Q_e). To this end, a new expression for the axial flow ratio (μ) that considers the torque (Q_e) is calculated using Eqs. (2.34), (2.53). In this calculation, (Q) is set to be equal (Q_e) instead of ($Q = 0$). This results in:

$$Q = \left(\tfrac{3}{2}\sigma\mu^2 + \varepsilon\sigma\mu - \tfrac{\delta\,\sigma}{4}\right)\pi\,R^5\,\rho\,\Omega^2 = Q_e \tag{2.64}$$

Substituting the expression of (Ω) from Eq. (2.63) to get:

$$\begin{aligned} \left(\tfrac{3}{2}\sigma\mu^2 + \varepsilon\sigma\mu - \frac{\delta\,\sigma}{4}\right) &= \frac{Q_e\sigma\left(\varepsilon + \dfrac{3}{2}\mu\right)\,\pi\,R^4\,\rho}{\pi\,R^5\,\rho\,W_d} \\ \Rightarrow\quad (1.5RW_d)\mu^2 + (R\varepsilon W_d - 1.5Q_e)\mu - (Q_e\varepsilon + 0.25R\delta W_d) &= 0 \end{aligned} \tag{2.65}$$

Now to investigate the energy harvesting possibility using the aforementioned model, a simulation model is constructed for this purpose to compute the aerodynamic forces, the aerodynamic coef-

ficients, the needed wind speed, the optimal values of the angle of incident (i), and the amount of energy and power can be harvested. In this simulation, all the constants coefficients involved in the calculations are assumed as follows: the number of blades ($B = 4$), blade radius ($R = 17.5\,ft$), blade chord ($c = 2.75\,ft$), and the total weight of the autogyro ($W = 1500\,lbs$). Furthermore, the value for the air density (ρ) at altitude of ($10\,km$) is set to be ($0.412\,kg/m^3 = 0.8{*}10^{-}3\,slugs/ft^3$). Other needed values are defined in Table 2.2. For all these parameter values, experimental validation was done in [Whe34].

Table 2.2: Autogyro Simulation Parameters

Parameter	**Value**
σ	0.2
ε	0.035 radians
ϖ_0	0.116
ξ	0.0024
η_1	0.02
η_2	0.01
δ	0.006

The simulation is first run for a pure autorotation mode of operation with ($Qe = 0$) and no generator load. The target thrust force ($W_d = 2000$) is chosen, ($W_d > W = 1500$). The results are shown in Fig. 2.10. Figure 2.10 (a) plots the steady state values of the drag and lift coefficients with respect to a varying angle of incidence (i), while Fig. 2.10 (b) shows the required amount of the wind relative velocity to generate the thrust force of ($W_d = 2000$) versus different values of angle of incidence (i). Subsequently, a new simulation with various values of (Q_e) is performed to study the effect of the energy extraction on the steady state operation of the autogyro. The values of the wind relative velocity associated with the same range of the angle of incident (i) that is used for the pure autorotation mode simulation, are shown in Fig 2.11 (a). It can be seen from these results that the required wind speed to handle the same amount of the thrust force ($W_d = 2000$) increases.

Furthermore, Fig 2.11 (b) shows that the values of the lift coefficient (L_C) decreases. The results also show that an effective lift force can be generated with an angle of incidence in the range of ($20 < i < 40$).

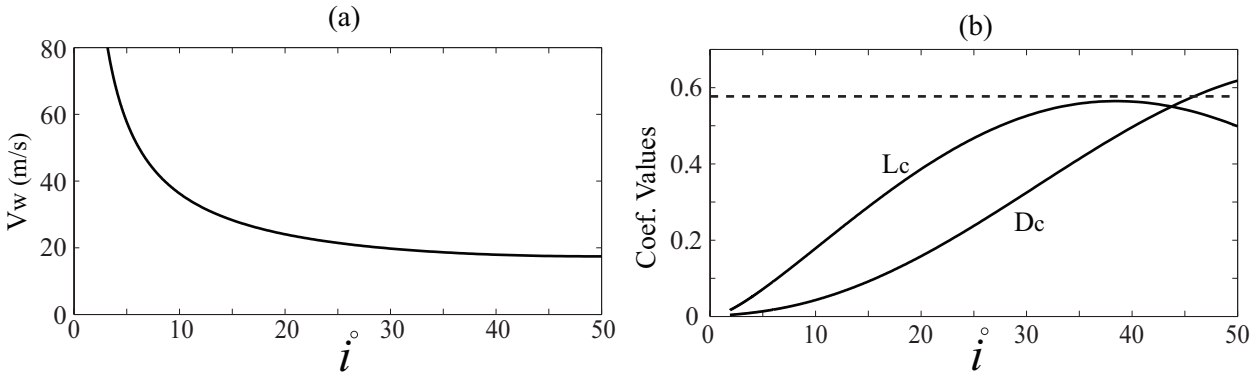

Figure 2.10: Steady State Autogyro, Simulation Results for $Q_e = 0$

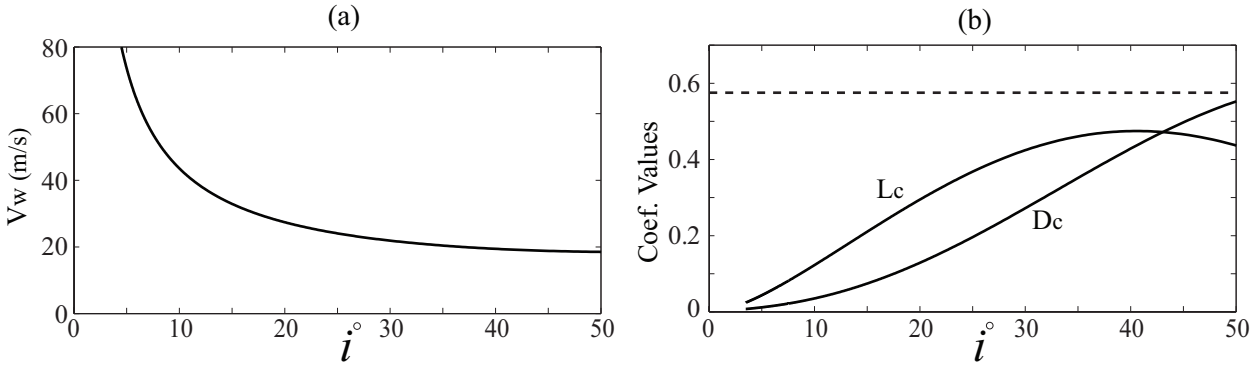

Figure 2.11: Steady State Autogyro, Simulation Results for $Q_e = 1000$

Finally, the amount of the extracted power for a range of (Q_e) values are calculated. The mechanical power values, computed using the expression of (Ω) in Eq. (2.63), are shown in Fig.2.12. Looking to the power extraction results, we can see that for ($Q_e = 1000$), an Autogyro system of weight ($2000\,lb$) can generate around ($\approx 28\,KW$) at an altitude of ($10\,km$).

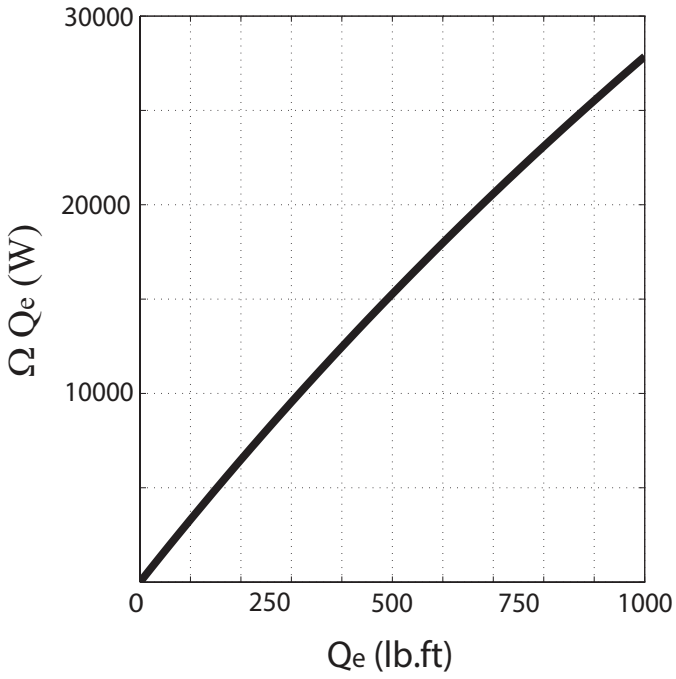

Figure 2.12: Steady State Autogyro, Mechanical Power

CHAPTER 3: DYNAMIC MODEL OF AUTOROTATION ENERGY SYSTEM

The previously discussed studies in Chapter 2 represent a good start for designing a system to generate energy from high altitudes, and provide encouraging results of the feasibility and viability of this approach. However, the introduced models lack of the dynamic analysis of untethered energy harvesting systems that need to be considered. Although having a tether prevents the flying systems from drifting away in the wind, operating a tethered system at high elevation would result in various issues regarding the stability of the system, and delay the control actions between the base and the flying part, especially the systems that need to move their flaying part in cretin way with respect to the motion of the base to extract energy. On the other hand, designing a rotor system with on board generator that uses tether in combination with autorotation principle, tethered autogyro system, could overcome the drawbacks of tethered systems. However, the high length tether would add a significant weight to this system, and need to access high altitudes of $(10 - 12\,km)$. Thus, the approach of using untethered autorotation-based system appears to be preferred for designing a system that is maneuverable and can simultaneously generate enough lift, harvest energy from a wind field, and remain enclosed within a bounded region in the atmosphere. This approach has several challenging aspects that need to be investigated such as launching, altitude controlling, lifting with the present of the generator weight, etc. Furthermore, the static analyses presented in chapter two are insufficient due to the continuous change in altitude, wind velocity, operating mode, environment properties, etc. Moreover, such a system for energy harvesting will eventually need to have an active altitude control. Therefore, the dynamic model of autogyro needs to be derived. This chapter presents the analyses of deriving an ideal but traceable dynamic model of the Autorotation Energy System (AES) that can be used to carry out the investigations on energy harvesting.

3.1 Autogyro System for Wind Energy Extraction - *Dynamic Analysis*

The steady state analyses of the autogyro system for energy harvesting presented in chapter two could potentially be utilized to drive a preliminary model that can express the dynamic state of AES. For this analysis, the aerodynamic forces and torques acting on the AES are assumed to be the same as those derived for the static model in chapter two. Mainly, we use the same expressions for all the aerodynamic coefficients. However, other expressions for the angular velocity and tip speed ratio are derived. Moreover, a different causality is used to drive the expression of the axial flow ratio. The AES model, used in the derivations, is assumed to be comprised of four identical blades with a large radius. These blades are connected to a single rotor and can rotate freely about their common shaft, $spinning$. The blades are also rotate about a hinge located at their roots in a direction normal to the shaft rotation axis, $flapping$. In addition, the system is assumed to be subjected to a strong wind field that flows through the blades to cause their rotation and produce the aerodynamic forces and torques needed for the system to flay. Furthermore, the center of effect of the thrust force, the longitudinal force, and the torque is considered to be coincide with the mass center of the system. Moreover, and due to equispaced blades, the periodic variation in the aerodynamic forces resulted from each blade at every instant is assumed to be neglectable. Also, the aerodynamic forces that act on the system in the lateral direction along the (Y) axis are assumed to be disregarded due to the inference that these forces can be canceled out if we place equal and opposite windmills in a future design. Consequently, the motion of the system is entirely within the (XZ) plane, and there is no movement along the (Y) axis. The system is also assumed to be ideally frictionless and all the friction forces between the bodies of the system are ignored.

3.1.1 Mathematical Model and Derivations

The proposed Autorotation Energy System (AES) consists of a windmill (f) with four blades ($B = 4$) that encounter a wind speed (V_w) and rotates with an angular velocity (Ω). AES has a total mass of (m_{AES}) with the center located at point (c) and moves with a translation speed (V_c). The blades have a radius (R) each, with their total mass representing only a (10%) of (m_{AES}). The aerodynamic forces and torques act on the system are the thrust force (T) along the shaft, the longitudinal force (H) at right angle to the thrust force (T) in in the plane of the shaft and the direction of motion, and the rotor torque (Q) about the shaft. The resultant forces acting on AES are the drag force (F_D) along the direction of the wind and the lift force (F_L) in a direction normal to the direction of the wind. The windmill (f) is inclined at angle of incident (i) that equals the summation of two angles: (θ) or the angle of inclination of the windmill (f) with the horizon and (γ) that represents the angle of the relative wind velocity (V_{rel}). Figure 3.1 shows a schematic diagram of AES.

Let ($OXYZ$) be a fixed frame of references at (O) with the bases [e_1, e_2, e_3], and let the vector (r_c) be the position vector of the mass center of AES with respect to ($OXYZ$). The position vector (r_c) is:

$$r_c = x_c\,\hat{e}_1 + x_c\,\hat{e}_3 \tag{3.1}$$

The velocity and acceleration equations are written respectively as:

$$V_c = \dot{z}_c\,\hat{e}_1 + \dot{z}_c\,\hat{e}_3 \tag{3.2}$$

$$a_c = \ddot{x}_c\,\hat{e}_1 + \ddot{z}_c\,\hat{e}_3 \tag{3.3}$$

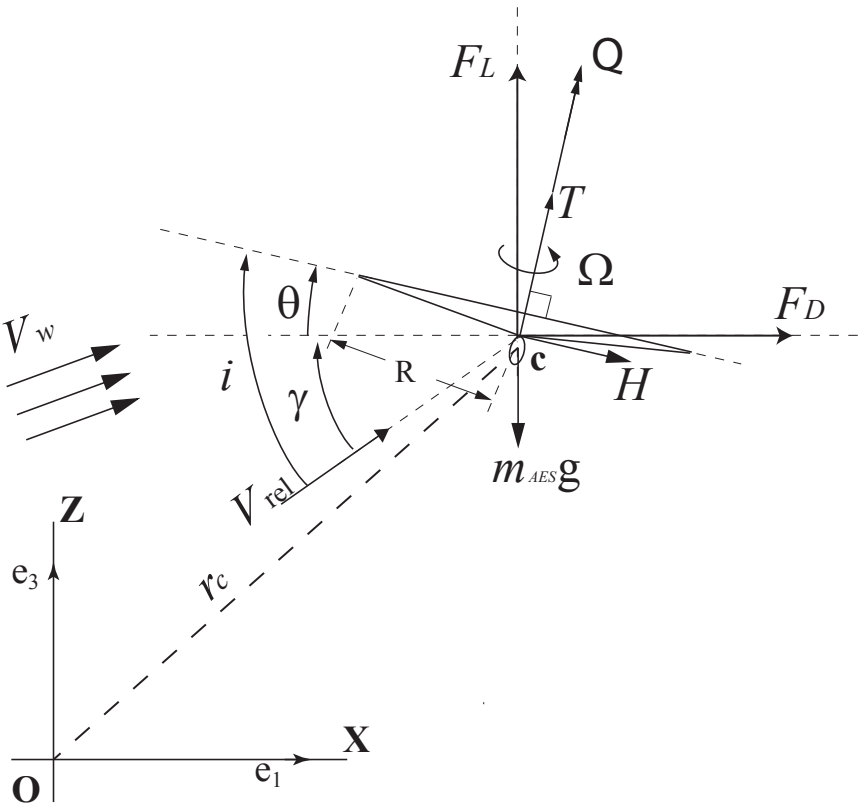

Figure 3.1: Forces Acting on (AES)

The wind velocity (V_w) is assumed to have two components, (V_{Wx}) along the (X) axis and (V_{Wz}) along the (Z) axis. Consequently the relative wind speed (V_{rel}) with respect to (V_c) is defined as:

$$\begin{aligned} & \vec{V}_{rel} = \vec{V}_w - \vec{V}_c = [\, V_{Wx} - \dot{x}_c \,] \,.\, \hat{e}_1 - [\, V_{Wz} - \dot{z}_c \,] \,.\, \hat{e}_3 \\ \Rightarrow \quad & \|\vec{V}_{rel}\|^2 = [\, V_{Wx} - \dot{x}_c \,]^2 + [\, V_{Wz} - \dot{z}_c \,]^2 \end{aligned} \tag{3.4}$$

and its direction can be obtained as:

$$\gamma = \tan^{-1} \frac{V_{Wz} - \dot{z}_c}{V_{Wx} - \dot{x}_c} \tag{3.5}$$

Considering all the forces and torques that act on AES, the system equations of motion are defined using Newton second low as the following:

$$m_{AES}\,\ddot{x}_c = T\,\sin\theta + H\cos\theta \tag{3.6}$$

$$m_{AES}\,\ddot{z}_c = T\,\cos\theta - H\,\sin\theta - m_{AES}g \tag{3.7}$$

$$I_s\,\dot{\Omega} = Q - Q_e \tag{3.8}$$

$$I_p\,\ddot{\theta} = Q_p \tag{3.9}$$

The (I_s) and (I_p) are the moment of inertia about the spin and pitch respectively. The moment of inertia (I_s) is considered to be constant since experimental data indicates that ($0 < \beta < 15^\circ$) [Whe34]. The parameter (Q_p) is the pitching control torque, while (Q_e) represents a braking torque provided by a generator that will be used later in energy harvesting analyses.

Defining the tip speed ratio as $\lambda = \dfrac{\Omega\,R}{V_{rel}}$, the expressions of ($T$), ($H$), and ($Q$) and all the corresponding coefficients are defined similar to those from the Eqs. (2.32), (2.49), (2.33), (2.59), (2.34), (2.53) as follows:

$$T = T_c\,\pi\,\rho\,\Omega^2\,R^4, \qquad T_c = \sigma\left(\varepsilon + \tfrac{3}{2}\mu\right) \tag{3.10}$$

$$H = H_c \, \pi \, \rho \, \Omega^2 \, R^4 \, .$$
$$H_c = \sigma \left[\tfrac{1}{2}\delta + \tfrac{8}{3}\varepsilon^2 + \tfrac{13}{2}\varepsilon\mu + \tfrac{9}{2}\mu^2 + \tfrac{1}{12}\varpi_0^2 + (8\eta_2 - 3\eta_1\varpi_0 - 24\eta_2^2 + \frac{1}{2}\xi \right] \frac{\cos i}{\lambda} \tag{3.11}$$

$$Q = Q_c \, \pi \, \rho \, \Omega^2 \, R^5 \, R \, , \qquad Q_c = \tfrac{\sigma}{4} \, (6\mu^2 + 4\varepsilon\mu - \delta) \tag{3.12}$$

3.1.1.1 Axial flow ration and Tip speed ratio calculations

The aforementioned derivations provide the necessary equations to calculate the aerodynamic forces (T, H, $and\, Q$). However, to be able to solve the equations, the expressions for the axial flow ration (μ) and tip speed ratio (λ) need to be derived. The derivation starts first by subtracting the two expressions of (T) from Eqs. (2.32) and (2.30). The result is as the following:

$$\begin{aligned} & T = T_c \, \pi \, \rho \, \Omega^2 \, R^4 \, \sigma \left(\varepsilon + \tfrac{3}{2}\mu \right) \, \pi \, R^2 \, \rho \, \Omega^2 \, R^2 \\ and \quad & T = (2\pi \, R^2 \, \rho \, V\prime \, \vartheta) \\ \Rightarrow \quad & \sigma \left(\varepsilon + \tfrac{3}{2}\mu \right) \, R^2 \, \Omega^2 = 2 \, V\prime \, \vartheta \end{aligned} \tag{3.13}$$

where ($V\prime$) is the resultant velocity experienced by the AES, while (ϑ) is the induced velocity. Using the expressions from Eqs. (2.31) and (2.38), we have:

$$\begin{aligned} & (\, V_{rel} \sin i \, - \, \vartheta) = \mu \, \Omega \, R \\ and \quad & V\prime = \sqrt{((V_{rel} \, \sin i - \vartheta \,)^2 + (V_{rel}^2 \cos^2 i)} \\ \Rightarrow \quad & V\prime = \sqrt{(\, \mu \, \Omega \, R \,)^2 + (V_{rel}^2 \cos^2 i)} \end{aligned} \tag{3.14}$$

Substituting Eq. (3.14) in Eq. (3.13) gives:

$$\begin{aligned} \Rightarrow \sigma \left(\varepsilon + \tfrac{3}{2}\mu\right)\, R^2\,\Omega^2 &= 2\,[\,V_{rel}\sin i\, - \mu\,\Omega\,R]\,[\sqrt{(\,\mu\,\Omega\,R\,)^2 + (V_{rel}^2\cos^2 i)}] \\ \Rightarrow \sigma\left(\varepsilon + \frac{3}{2}\mu\right) &= 2\,[\,\frac{V_{rel}\sin i}{\Omega\,R}\, - \mu\,]\,[\sqrt{(\,\mu^2\,) + \frac{V_{rel}^2\cos^2 i}{\Omega^2\,R^2}}] \end{aligned} \tag{3.15}$$

By squaring both sides of the equation and using the expression of (λ), we get:

$$\begin{aligned} \Rightarrow [\sigma\,\varepsilon + 1.5\,\mu]^2 &= 4\,[\,\frac{\sin i}{\lambda}\, - \mu\,]^2\,[(\,\mu^2\,) + \frac{\cos^2 i}{\lambda^2}] \\ \Rightarrow \sigma^2\,\varepsilon^2 + 3\,\sigma^2\,\varepsilon\,\mu + 2.25\,\sigma^2\,\mu^2 &= 4\,\mu^4 + 4\,\frac{\cos^2 i}{\lambda^2}\,\mu^2 \\ +4\,\frac{\sin^2 i}{\lambda^2}\,\mu^2 + 4\,\frac{\sin^2 i\,\cos^2 i}{\lambda^4} - 8\,\frac{\sin i}{\lambda}\,\mu^3 - 8\,\frac{\sin i\,\cos^2 i}{\lambda^3}\mu & \end{aligned} \tag{3.16}$$

and by rearranging Eq. (3.16), we get the following forth order equation:

$$[\,4\,]\,\mu^4 - [\,8\,\frac{\sin i}{\lambda}\,]\,\mu^3 + [\,\frac{4}{\lambda^2} - 2.25\,\sigma^2\,]\mu^2 - [8\,\frac{\sin i\,\cos^2 i}{\lambda^3} + 3\,\sigma^2\,\varepsilon\,]\mu + [4\,\frac{\sin^2 i\,\cos^2 i}{\lambda^4} - \sigma^2\,\varepsilon^2\,] = 0 \tag{3.17}$$

Equation (3.17) depends on three parameters ($\mu,\ \lambda,\ and\, i$), and to get a solution for (μ) or (λ), we need to provide the angle of incident (i) and either (μ) or (λ). However the goal of this derivation is to find the expressions that define (μ) and (λ). Therefore, we identify two suitable ranges for the values of (λ) and (i), and then solve the forth order Eq. (3.17) with respect to (μ). Subsequently, we create a three dimensional surface that can provide a value of one of the parameters, (μ) or (λ), if the values of (i) and the other parameter ore substituted. To solve the equation, we use the following constants values: ($\sigma = 0.2$), ($R = 5.334\,m$), and ($\varepsilon = 0.035\ radians$). Figure 3.2 shows the set of solutions of this equation.

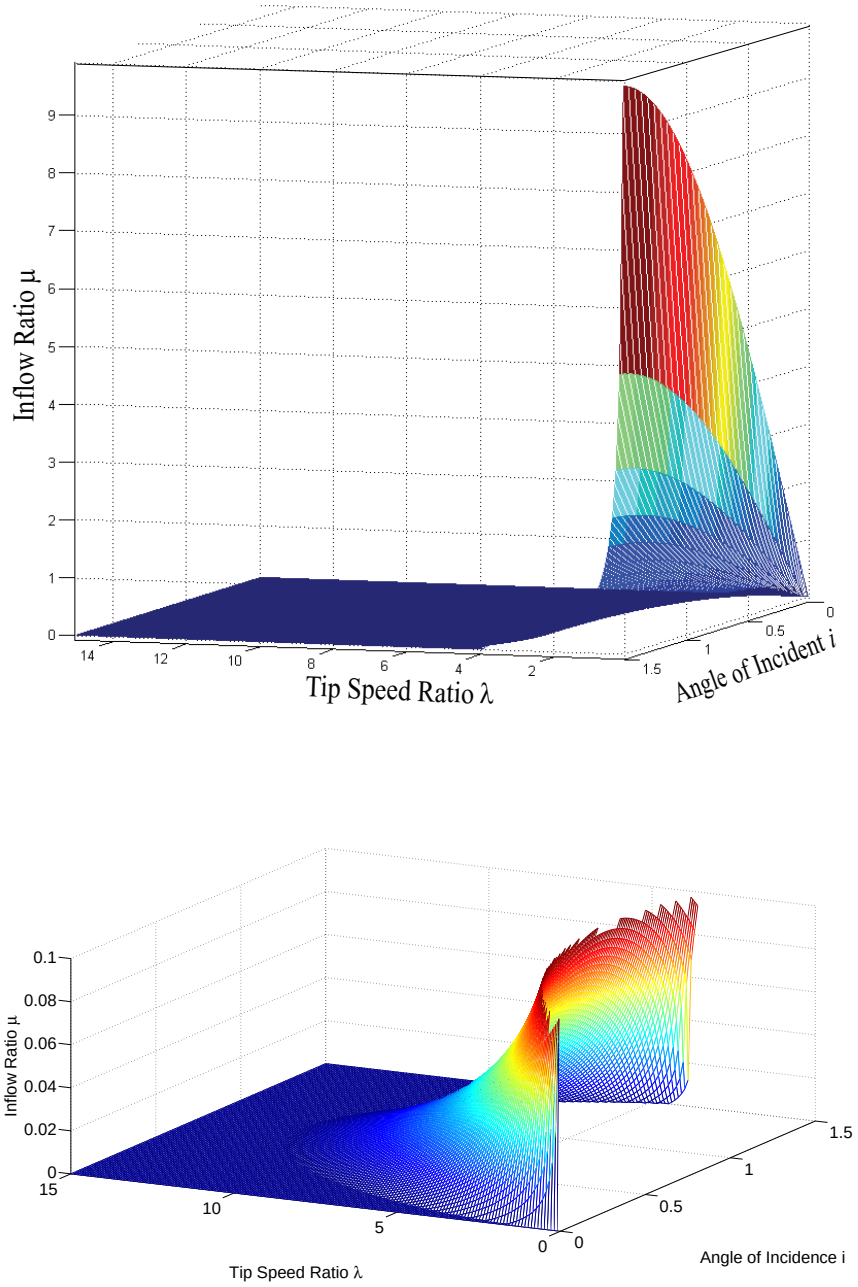

Figure 3.2: 3D Mesh Surface Represents the Solution of Eq. (3.17)

3.2 Model Simplifications

For the seek of simplicity, some assumptions have been made to the AES model before carrying out the simulation. First of all, the system is assumed to have only the angular velocity about the shaft (Ω) and there is no rotational motion about any other direction ($\ddot{\theta} = 0$). However, the angle (θ) is assumed to be controlled in a way that we can change its value when needed. Furthermore, an expression for the axial flow ratio (μ) is derived to simplify the solution of the forth order Eq. (3.17) and find a relation between the angle (i) and the tip speed ratio (λ). The windmill (f) has only (10%) of the total mass, thus its moment of inertia (I_s) is small compared to the resultant forces and moments acting on the system. Consequently, this derivation approach, referred to in this thesis as the $Static\,\mu$ approach, defines (μ) under the assumption that the windmill moment of inertia (I_s) is neglectable. Therefore Eq. (3.8) with ($Q_e = 0$) gives ($Q = 0$). Then the positive (μ) is calculated as:

$$\begin{aligned} Q = &\quad B\,c\,\rho\Omega^2\,R^4\tfrac{1}{4}\,(6\mu^2 + 4\varepsilon\mu - \delta) = 0 \\ \Rightarrow &\quad \tfrac{1}{4}\,(6\mu^2 + 4\varepsilon\mu - \delta) = 0 \\ \Rightarrow &\quad \mu = \tfrac{1}{3}\left[\sqrt{\varepsilon^2 + \frac{3}{2}\delta} - \varepsilon\right] \end{aligned} \tag{3.18}$$

Resolving the ($\mu,\ \lambda,\ and\, i$) forth order equation expressed in Eq. (3.17) with considering the expression of the ($Static\,\mu$) from Eq. (3.18) leads to have a direct relation (curve) between (λ) and (i) as shown in Fig. 3.3.

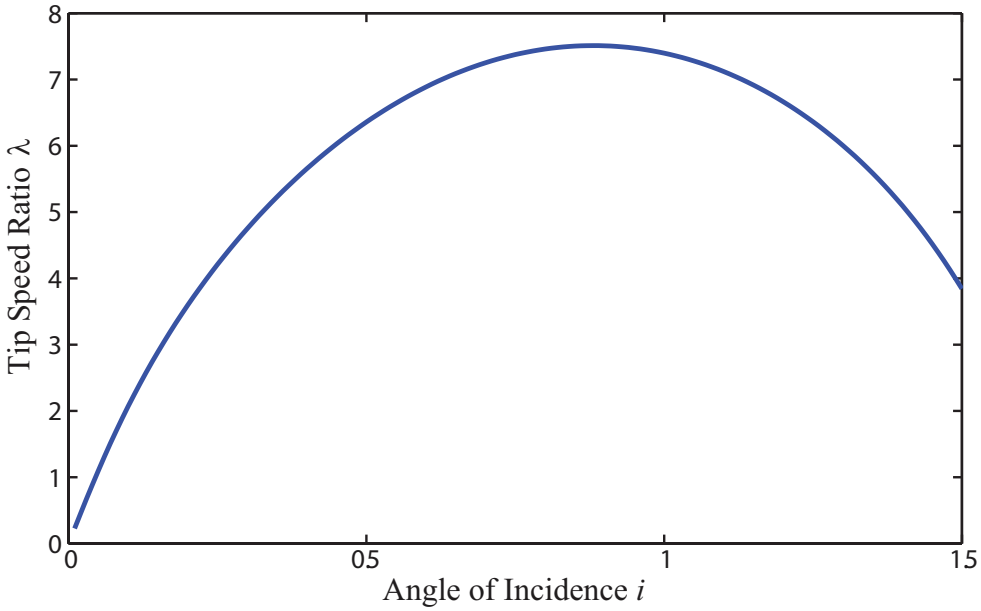

Figure 3.3: (i) and (λ) Relation Curve

Additionally, the system is assumed to be subjected to a horizontal wind with only one component along the (X) axis; therefore, (V_{rel}) is redefined as shown in Eq. (3.19). The angular velocity (Ω) is also redefined based on the tip speed ratio (λ) as shown in Eq. (3.20).

$$\|\vec{V}_{rel}\|^2 = [\, V_{W\,x} - \dot{x}_c \,]^2 + [\, \dot{z}_c \,]^2, \qquad \gamma = \tan^{-1} \frac{-\dot{z}_c}{V_{W\,x} - \dot{x}_c} \tag{3.19}$$

$$\Omega = \frac{V_{rel}}{\lambda\, R} \tag{3.20}$$

Finally, the longitudinal force (H) is assumed neglectable, and the only force that act on AES is the thrust force (T). This assumption is made based on the simulation results of the static model presented in the study [RD13]. It can be observed from these results that the magnitude of the

longitudinal force (H) equals at maximum (10%) of the thrust force (T) as shown in Fig 3.4. Therefore, the effect of (H) on the dynamic behavior of the system is assumed small compared with the effect of (T). Consequently, the force (H) is ignored, and the system equation of motions (3.6) and (3.7) are modified as shown below. In addition, the force (T) is set to zero if the angle of incident becomes either smaller than (3°) or larger than (90°), and this is because of the fact that the system's mode is no longer autorotation mode, and the thrust force (T) is no more generated.

$$m_{AES}\,\ddot{x}_c = T\,\sin\theta \tag{3.21}$$

$$m_{AES}\,\ddot{z}_c = T\,\cos\theta - m_{AES}g \tag{3.22}$$

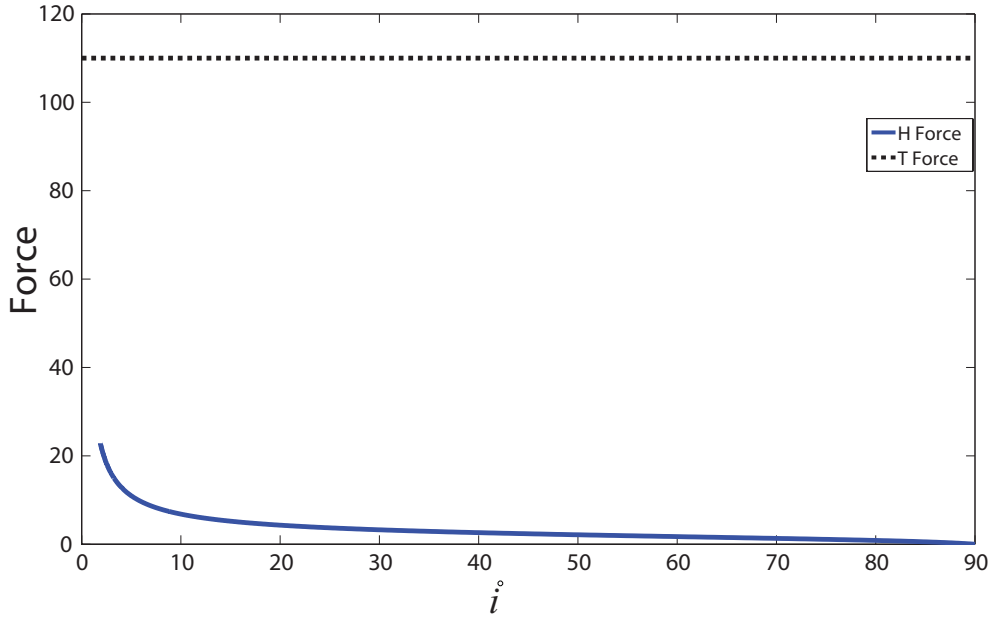

Figure 3.4: (H) and (T) Forces

3.3 Energy Harvesting Analysis

In order to utilize the AES in harvesting energy from high altitude, an electrical generator needs to be added to the system. This generator is assumed to be attached to the shaft of the system's rotor, and driven by the mechanical power provided by the windmill (f). The amount of the power and energy produced by a generator is usually calculated based on the generator's voltage and current. However, in this level of investigation, the generated power and energy are measured based on the mechanical power needed to be provided to derive the generator. For our analyses, a braking torque (Q_e) is considered to represent the additional amount of the load that added to the system due to the attached generator. Consequently, the mechanical power is calculated based on this braking torque and the angular velocity of the wind mill as follows:

$$P_{ext} = Q_e\,\Omega, \quad W(J/s) \tag{3.23}$$

The extracted power is then integrated over the time to compute the produced energy in ($Joule$).

$$E_{ext} = \int_0^t P_{ext}\,dt \tag{3.24}$$

In all the above calculations, the efficiency of the used generator is assumed to be ideally 100%. By incorporating the braking torque (Q_e) in the dynamic motion of the AES system, the assumption of considering ($Q = 0$) due to neglecting (I_s) in Eq. (3.8) is no longer valid. Thus, the $Static\,\mu$ approach that is used to derive the static expression of the axial flow ratio (μ) in Eq. (3.18) is no more applicable. Therefore, we use anew approach that calculates (μ) based on the angular velocity of the system (Ω), and referred to in this thesis as the $Dynamic\,\mu$ approach. Consequently, the

angular velocity (Ω) is calculated first using the equation of motion (3.8) as follows:

$$\begin{aligned} \dot{\Omega} &= \frac{Q - Q_e}{I_s} \\ \Rightarrow \quad \Omega &= \int_0^t \dot{\Omega}\, dt \end{aligned} \tag{3.25}$$

where the aerodynamic torque (Q) is defined in Eq. (3.12). Subsequently, the tip speed ratio (λ) is calculated based on (Ω) as shown in Eq. (3.26)

$$\lambda = \frac{\Omega\, R}{V_{rel}} \tag{3.26}$$

Thus, the value of (μ) can now be calculated using the three dimensional surface shown in Fig 3.2 by using the angle (i) and the value of (λ).

CHAPTER 4: SIMULATION ANALYSIS AND RESULTS

In this chapter, the dynamic model of the Autorotation Energy System (AES) is examined using a simulation testbed written in Matlab. The dynamic behavior of the system is investigated to explore the rudimentary maneuvers of AES, and obtain a through understanding about the response of AES to the different parameters that affect its model. We first illustrate the approaches and schemes that are used in the simulation. Then the performance results and comparisons are presented and discussed.

4.1 Simulation Details

In order to carry out simulation tests on the AES model, the values of the constant parameters involved in the calculations are defined as follows: number of the blades ($B = 4$), blade radius ($R = 5.334\,m$), blade chord ($c = 0.8382\,m$), and total weight ($W = 50\,kg$). The speed of the wind is specified using the probability distribution of wind power density shown in Fig 1.4 (c). It can be observed that there is a (65%) probability of achieving $P_{w,den} = 1.5\,kW/m^2$ at an altitude of ($10\,km$). Therefore, we can use the relation ($P = 0.5\rho V^3$) and the value of the air density at ($10\,km$), $\rho = 0.412\,kg/m^3$ to calculate the speed of the wind at this elevation. Consequently, we conclude that there is a (65%) probability of achieving ($V_W \approx 19\,m/s$). Thus, in our calculation, the speed of the wind is assumed to be equal ($V_W = 15\,m/s$). Different values are also assigned to the angle of the windmill inclination (θ) based on the simulated case. Other needed values are defined in Table 4.1. For all these parameter values, experimental validations were done in [Whe34]. Unless different values are specified, the mentioned parameters are used as default values for all the simulation's results presented in this chapter.

Table 4.1: AES Simulation Parameters

Parameter	**Value**
σ	0.2
ε	0.035 radians
ϖ_0	0.116
ξ	0.0024
η_1	0.02
η_2	0.01
δ	0.006

4.2 Simulation Results of a Pure Autorotation Mode

To investigate the dynamic behavior of the AES under autorotation flight conditions, an initial set of simulations is run first using the $Static\,\mu$ approach, and without considering any generative braking torque ($Q_e = 0$). For this mode of operation, different results are shown using different hovering scenarios. The system is assumed to have an inboard control mechanism that can be used to change the value of the windmill's angle of inclination with the horizon, (θ).

4.2.1 Free Falling

In this hovering scenario, the model is left to fall while subjected to the wind. The angle (θ) is set to $zero$ as shown in Fig 4.1, then the model is simulated to get an idea about its flying distance, and compute the translating velocity, the angular velocity of the windmill, the magnitude and direction of the wind relative velocity, all as functions of time. The results are shown below in Figs 4.2 (a-f).

The simulation results of this scenario show a steady state behavior. From Fig 4.2 (a), it appears that the system is falling down vertically and there is no motion along the (x) axis, and this is due to the assumption of neglecting the longitudinal force (H) and setting (θ) to $zero$.

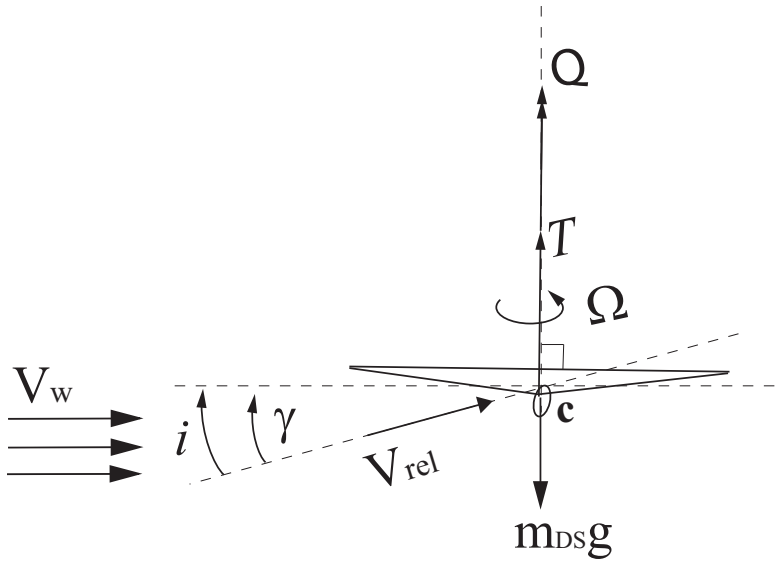

Figure 4.1: Schematic of Free Falling Scenario

This behavior can be also confirmed analytically by solving the model equations of motion (4.1), and (4.2):

$$m_{AES}\,\ddot{x}_c = T\,\sin\theta \tag{4.1}$$

$$m_{AES}\,\ddot{z}_c = T\,\cos\theta - m_{AES}g \tag{4.2}$$

When (θ) equals to $zero$, then $\ddot{x}_c = 0$ and $\ddot{z}_c = \frac{T}{m_{AES}} - g$. Consequently, the steady solution leads to have the following result: $\dot{x}_c = x_c = 0$ and $\dot{z}_c = -1.506\,m/s$. Although, the windmill is set to be horizontal and be subjected to the wind with no inclination, it rotates with an angular velocity and generates a thrust force because of the direction of the wind relative velocity (V_{rel}) with respect to the horizontal axis that sustains an angle of incident ($i = \gamma$) as shown in Figs 4.2 (c, e, and f).

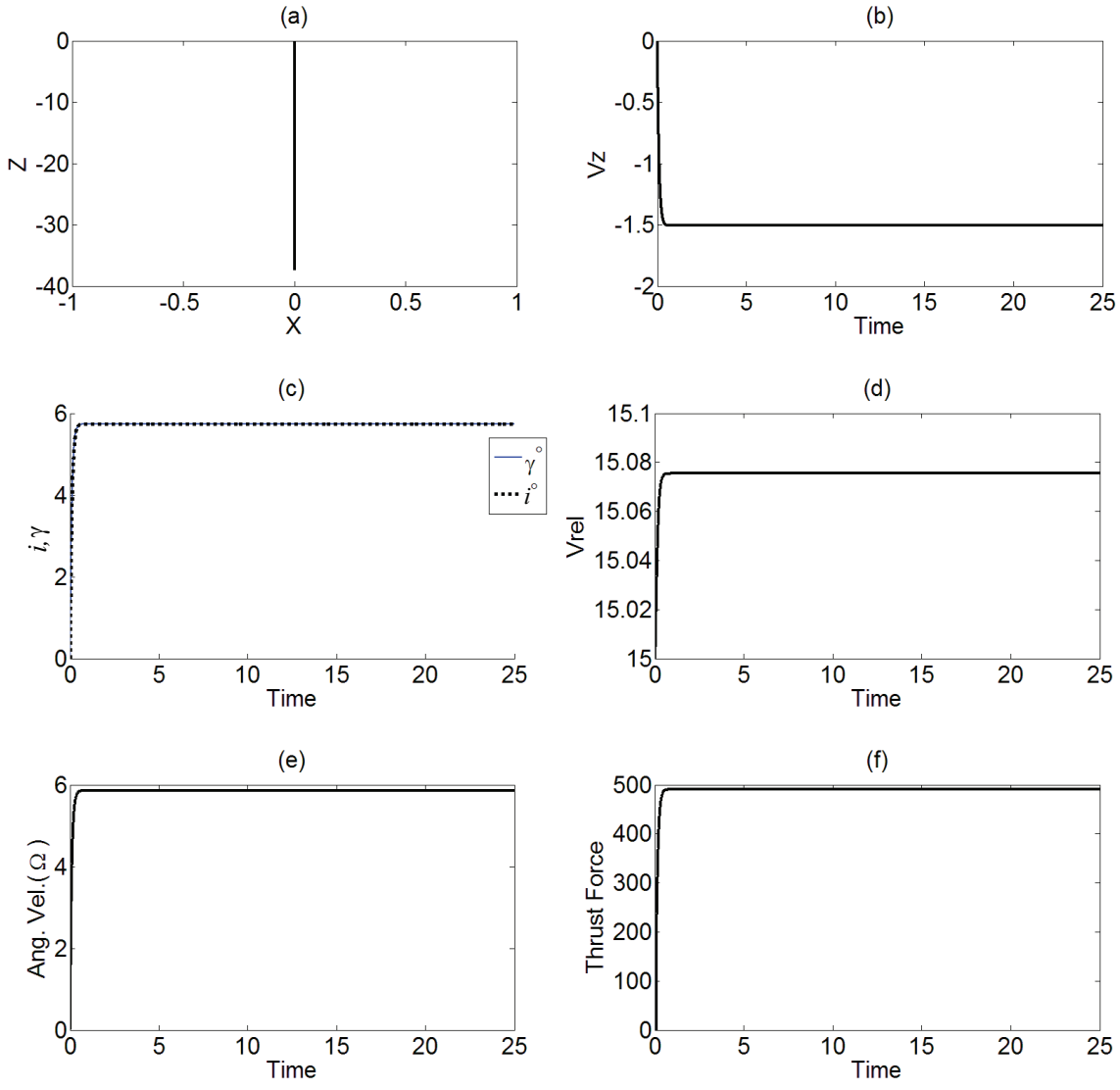

Figure 4.2: Pure Autorotation Mode: Free Falling Scenario

It can be observed from the direction of the relative velocity (γ), that the mode of operation is an autorotation mode, and the relative velocity flows throw the windmill of the system from the bottom as shown in in Fig 4.1. See Eq. (4.3).

$$\gamma = \tan^{-1} \frac{-\dot{z}_c}{V_{Wx} - \dot{x}_c} \tag{4.3}$$

By referring to the Eq. (4.3) with $\dot{x}_c = 0$ and a constant value of (V_W), it can be observed that the angle (γ) is mainly effected by the velocity along the (Z) axis, (V_z) that is maintained by the system weight. Therefore, in this flight scenario, increasing the weight of the system changes the direction of the relative wind speed, and enlarges the angle of incident (i) that lead to have a higher angular velocity (Ω) and a larger thrust force (T). Figures 4.3 (a-d) show the forces, velocities, and angle of incident of the system for various masses values.

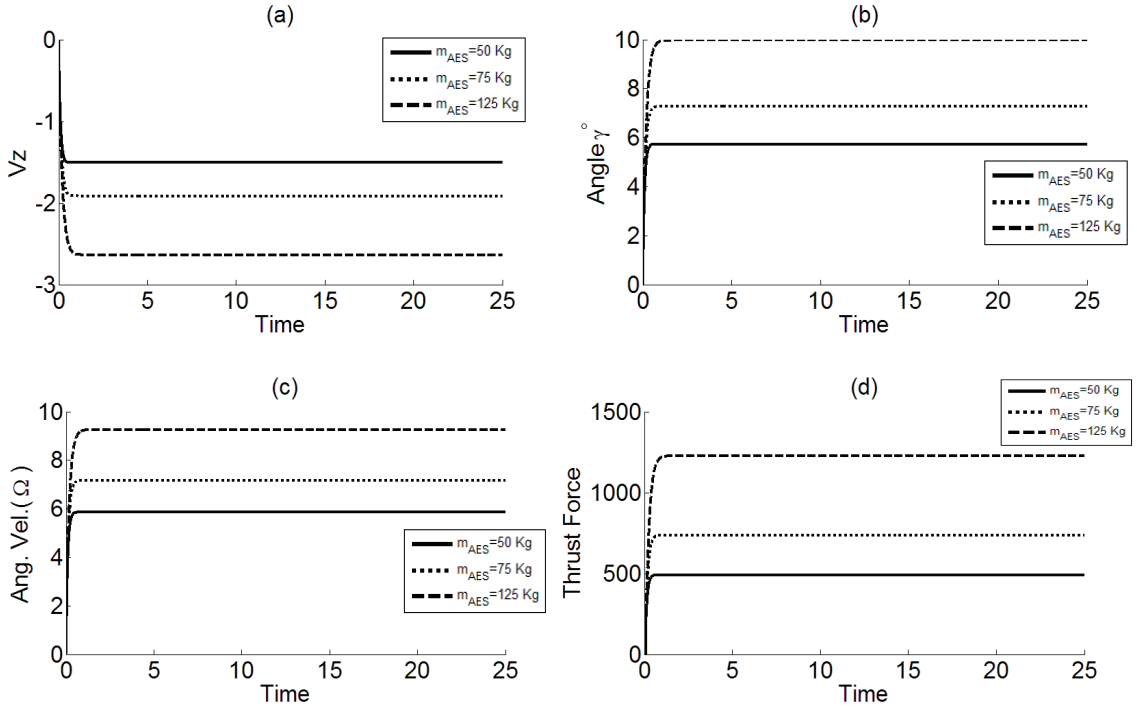

Figure 4.3: Free Falling Flight with Different Masses

4.2.2 *Flying Against the Wind*

Another set of simulations is carried out for negative values of the angle (θ). For this flying scenario, the windmill is assumed to be tilted by a small negative angle (θ) as shown in Fig 4.4, and then the system is simulated.

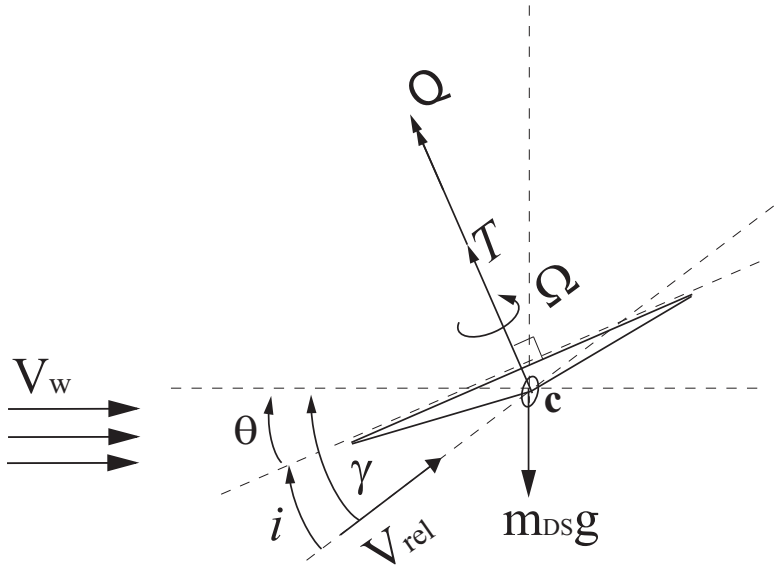

Figure 4.4: Negative Angle (θ) Scenario Schematic

Figure 4.5 (a) shows the simulation's result of the system's motion in the (XZ) plane for three negative angle values ($\theta = -4, -8, -10°$). This result confirms the ability of the system to move against the wind under the autorotation mode operation; however, the system keeps falling dawn and there is no gained lift along the positive (Z) direction. In addition, it can be observed from Fig 4.5 (a), that the velocity of the system increases by increasing the angle (θ) in the negative direction. For the same period of simulation's time, the system travels along a higher distance when the windmill is tilted by a higher negative angle (θ). The autorotation mode of operation for this scenario can be confirmed by examine the angle (γ) associated with each one of the three

negative angle (θ)'s values ($-4, -8, -10°$). From Fig 4.5 (b), it can be seen that all the values of (γ) are higher than their corresponding values of (θ). Therefore, these results confirm that the relative velocity flows throw the windmill of the system from its bottom to the top as show in Fig 4.4.

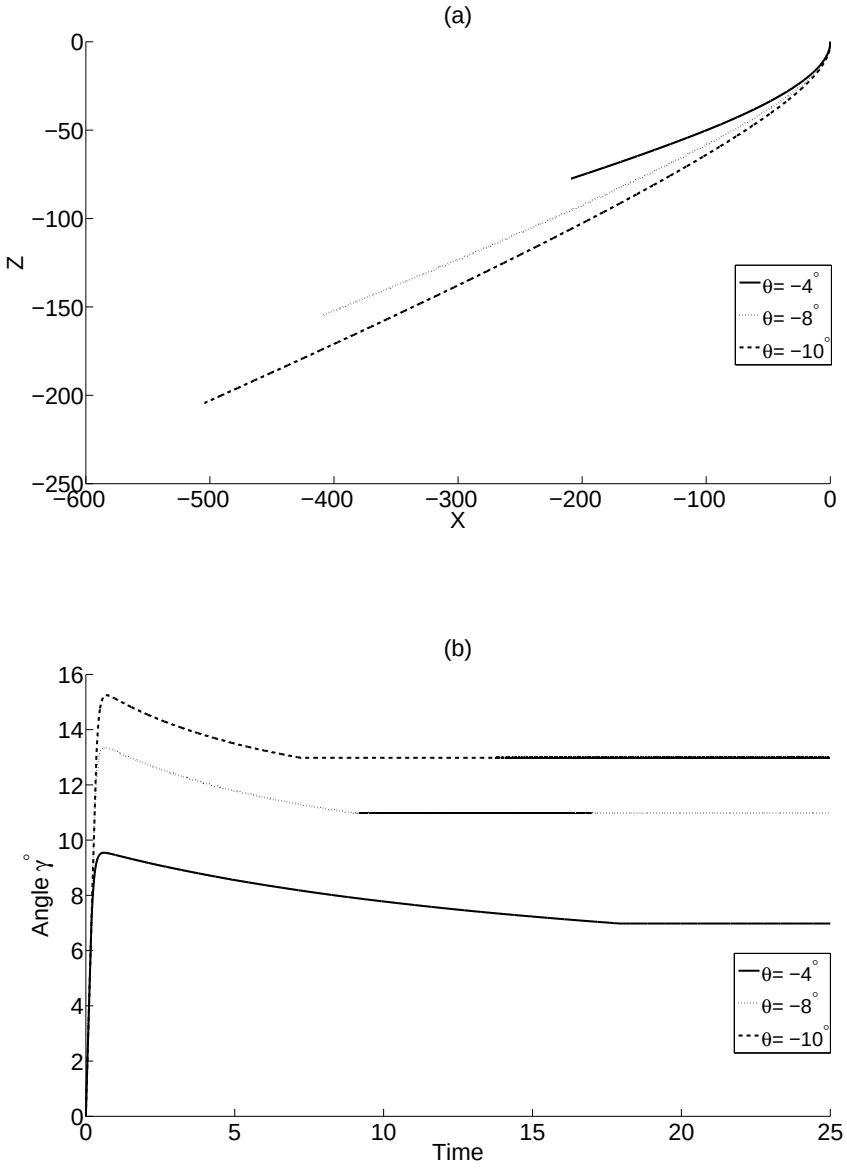

Figure 4.5: Flying Against the Wind with Variable (θ): System Positions and Angle (γ)

The simulation's results of the other parameters for the angle ($\theta = -4^{\circ}$) are also presented below. These results show an instability in the behavior of the system especially its velocity in the (X) direction. The magnitude of the relative velocity increases rapidly because of the continuous raise of (Vx) and thus affects the angular velocity and the thrust force. However the angle (γ) tends to have a small range of constant values. Figures 4.6 (a-d) show the position and the velocity of the system along the (X) and (Z) directions, while Figs 4.7 (a-d) show the results of the (V_{rel}), (γ), (i), (Ω), and (T).

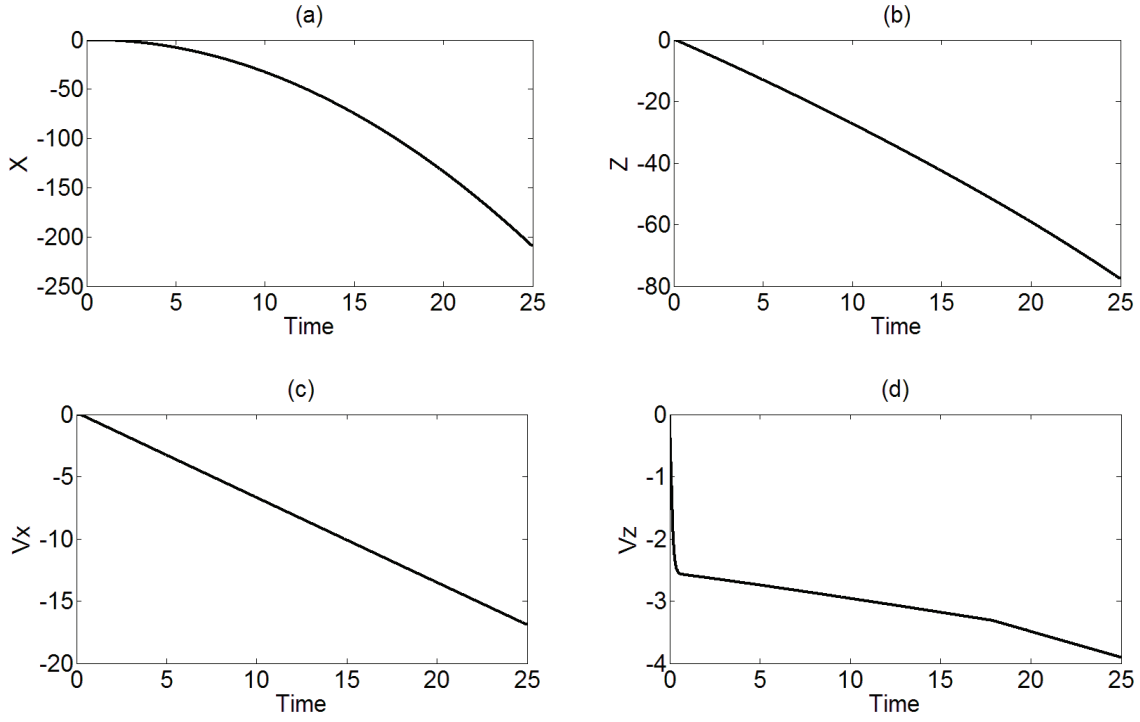

Figure 4.6: Flying Against the Wind Scenario: Positions and Velocities of the System

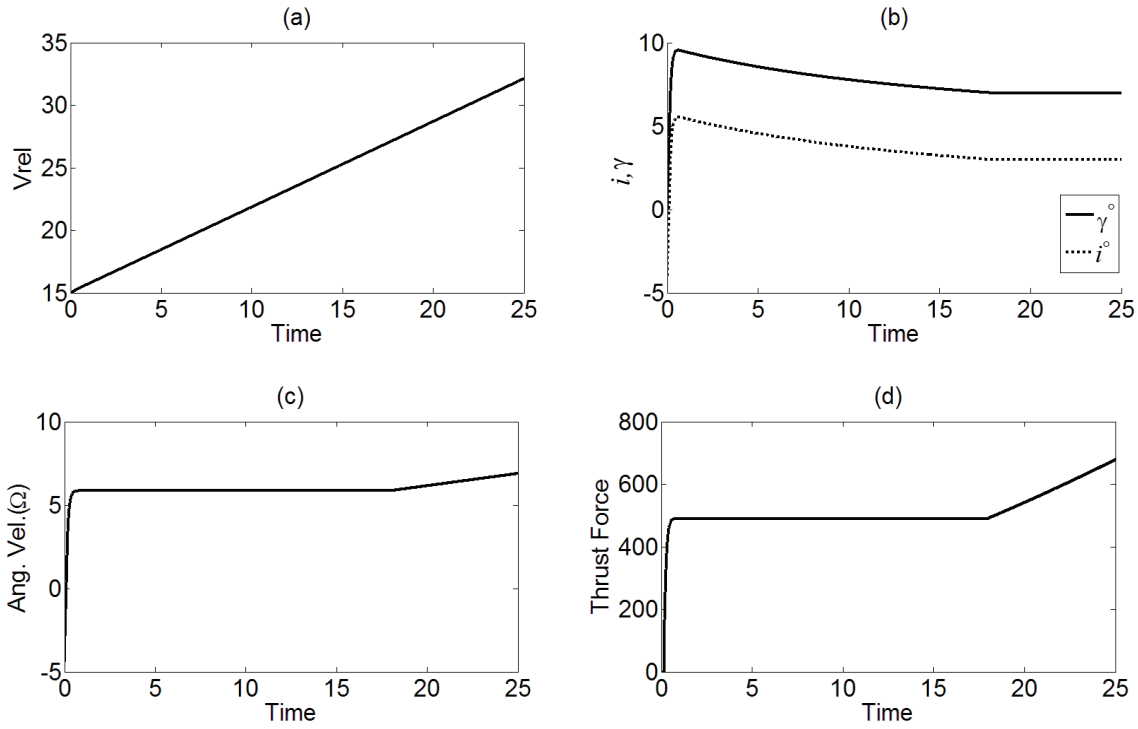

Figure 4.7: Flying Against the Wind Scenario: Force, Angles, and Angular Velocity of the System

4.2.3 Flying with the Direction of the Wind

The scenario, in which the windmill is inclined by positive values of angle (θ) with respect to horizontal axis as shown in Fig 4.8, is also investigated. For this simulation case, three positive values are assigned to the angle (θ). The simulation time is set to be identical in all the three simulation runs. Figures 4.9 and 4.10 show the results of the system position, and the angle of incident (i) corresponding to the three angle's values ($\theta = 4, 8, 10^{\circ}$) respectively.

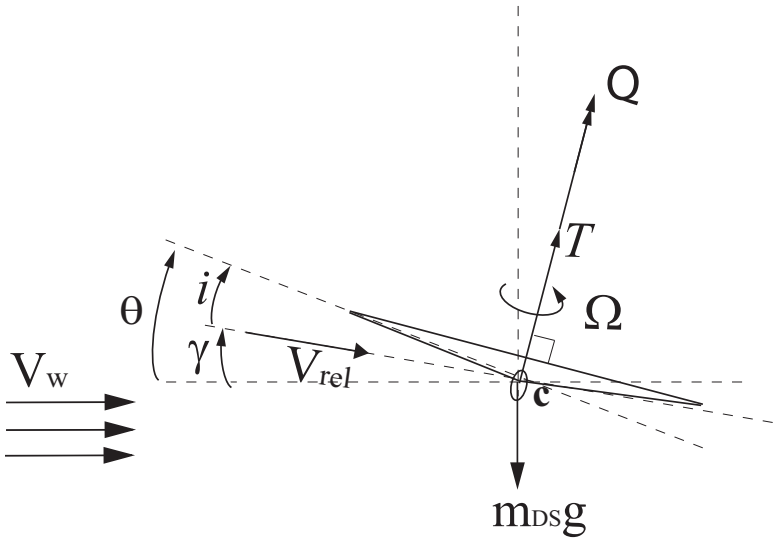

Figure 4.8: Positive Angle (θ) Scenario Schematic

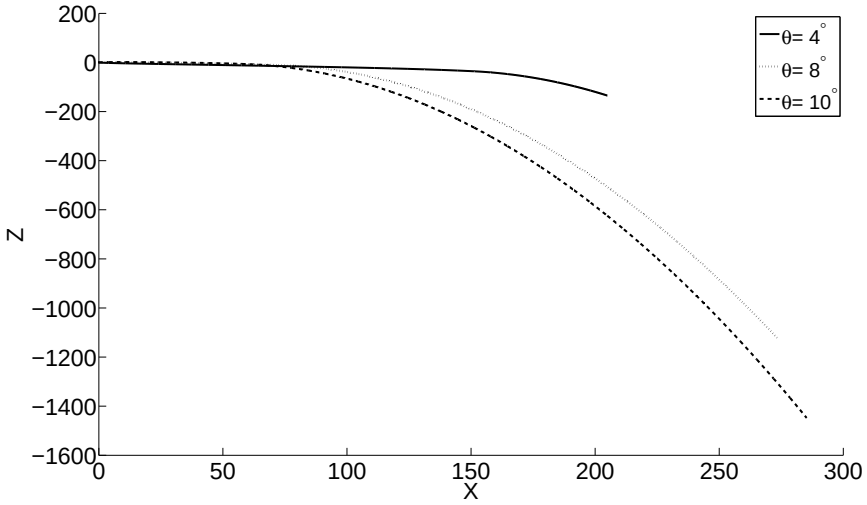

Figure 4.9: Flying with the Wind Scenario: System Position Results For Variable (θ)

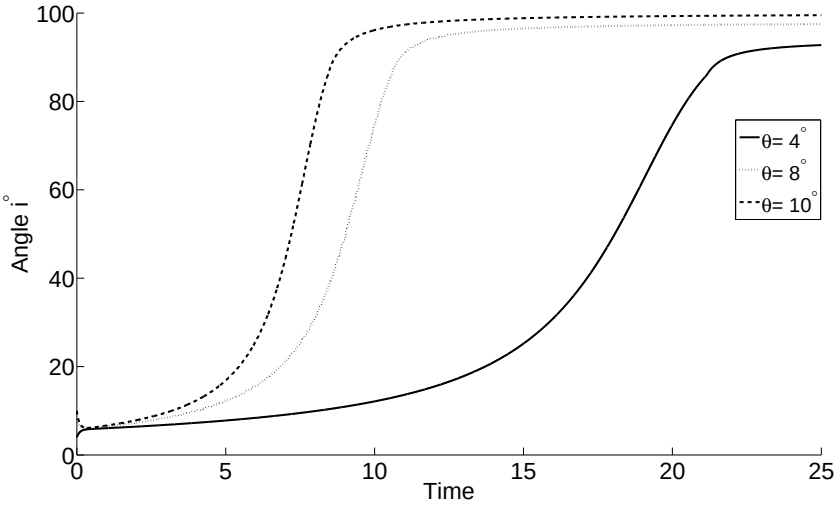

Figure 4.10: Flying with the Wind Scenario: Angle of Incident (i)

The AES's ability of flying with the direction of the wind is confirmed by the simulation's results presented in Fig 4.9. However, these results indicate the instability in the behavior of the system when the angle (θ) is set to be positive. Although, the system starts hovering under Autorotation mode, the velocity of the system, especially in the (Z) direction, starts getting a large increase in its magnitude after a small period of operation time (simulation time). Therefore, the angle of incident (i) gets a significant increase in its value, see Figs 4.9 and 4.10. Furthermore, it can be observed that the time of reaching instability decreases with the increase in the value of angle (θ), and the system tends to have unstable flying even with the small angle ($\theta = 4^{\circ}$). Figures 4.11 (a-h) show the system position, the system velocities, the thrust force, and the relative velocity, all corresponding to the angle ($\theta = 4^{\circ}$). By examining these results, we can see that when the simulation's time reaches the second (20), the flaying mode is no longer autorotation mode. The angle (γ) starts reaching (90°), thus the force (T) becomes $zero$ due to the predefined condition ($4^{\circ} < i < 90^{\circ}$).

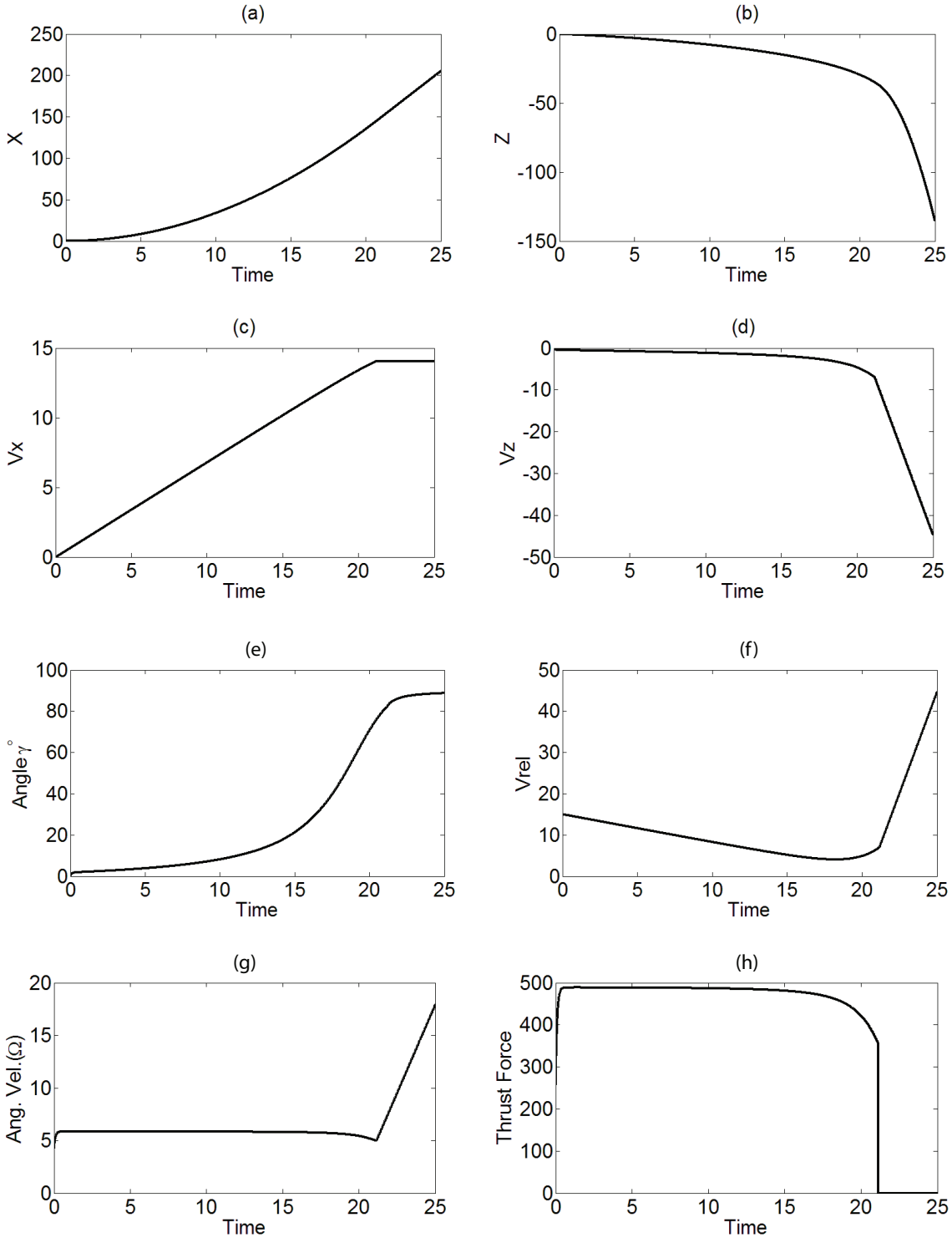

Figure 4.11: Flying with the Wind Scenario: Results Associated with Angle ($\theta = 4°$)

4.2.4 *Maneuvering with Varying Angle (θ)*

During the free falling scenario, the system reaches a steady state behavior; however, it can be observed from the second and third scenario's results presented in subsections (4.2.2) and (4.2.3) respectively, that the proposed dynamic model for AES needs an active and continuous control to be able to maintain a steady state flight conditions. Furthermore, the results confirm the ability of the system to fly either with or against the direction of the wind. The system's trend of moving in opposite directions can be utilized to reduce the velocity of the system and thus affects its other parameters. Therefore, another two simulation's sets are carried out using variable values for the angle (θ). In these simulation schemes, the system is assumed to have an active control mechanism that can change the angle (θ) continuously using either positive, negative, or zero values based on the speed and position of the system as shown in the schematic presented in Fig 4.12.

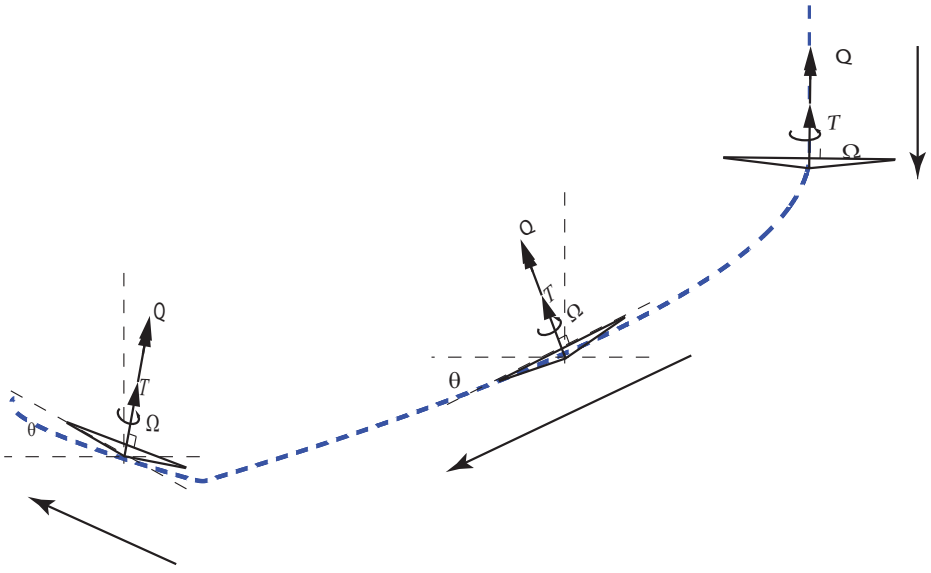

Figure 4.12: Flying with Variable Values of (θ) Schematic

We refer to the first flaying scheme by $Falling\ Against\ the\ Wind$. In this scheme, the angle (θ) is sequentially changed to the following values ($0, -4, 10^{\circ}$). We first set (θ) to $zero$ and run the simulation for ($11\ s$). Then (θ) is changed during the simulation to (-4°) and left for another ($13\ s$). Finally, the angle (θ) is changed to (10°) for ($6\ s$). Figure 4.13 shows the changes in the ($x - z$) plane position of the system during this simulation run.

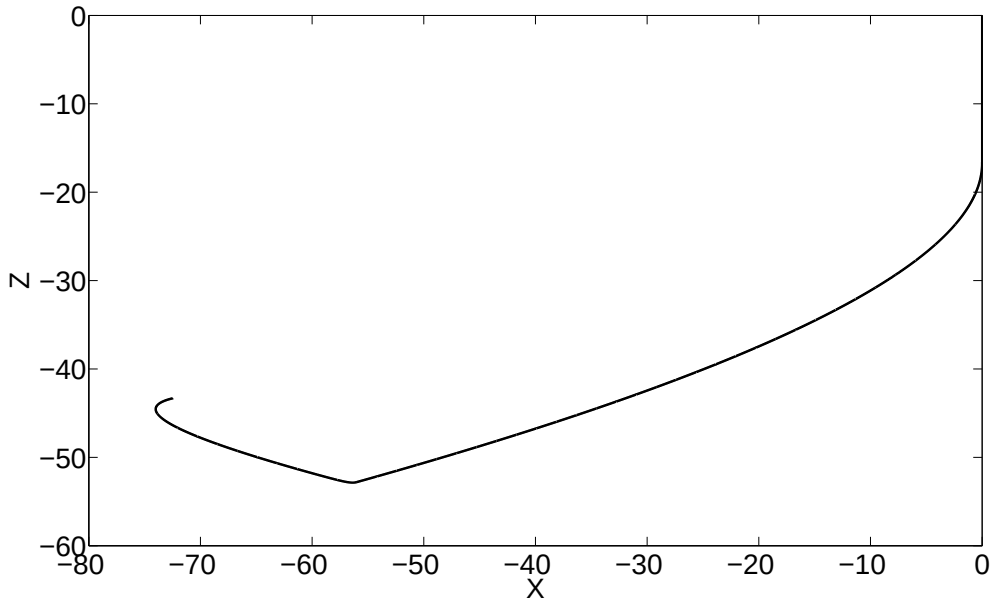

Figure 4.13: Falling Against the Wind Scheme:($x - z$) Positions

The dynamic behavior of the system during this simulation run is as expected. The system falls dawn when (θ) is set to $zero$, then the system flies against the wind when (θ) is changed to a negative value. Furthermore, setting (θ) to a positive value causes the system to reduce its resultant velocity as shown in Figure 4.14, due to the trend of the system to fly in the same direction of the wind.

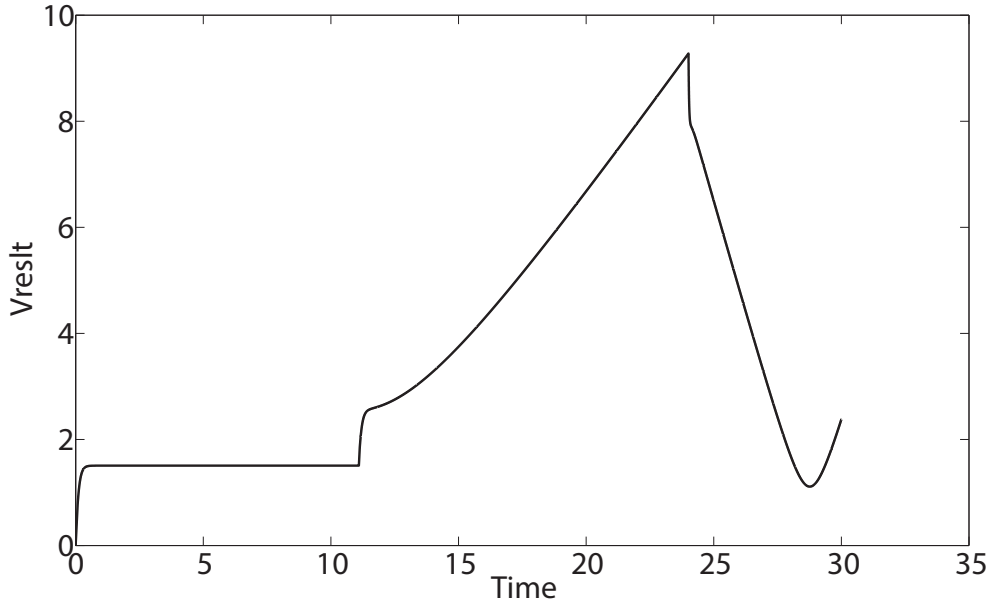

Figure 4.14: Falling Against the Wind Scheme: Resultant Velocity

Another simulation scheme is carried out for $(60\,s)$ using different values of the angle (θ). This scheme is referred to by $Falling\,with\,the\,Wind$. In the first $(10\,s)$ of the simulation run, the angle (θ) is set to $zero$, then it changed to a positive value (4°) and the system flies in the direction of the wind for $(15\,s)$. However, once the angle (θ) is set to a negative angle (-8°), the flying direction becomes against the wind. Finally, the angle (θ) is set again to a positive value (8°) to control the velocity of the system. The result is shown in Fig 4.15.

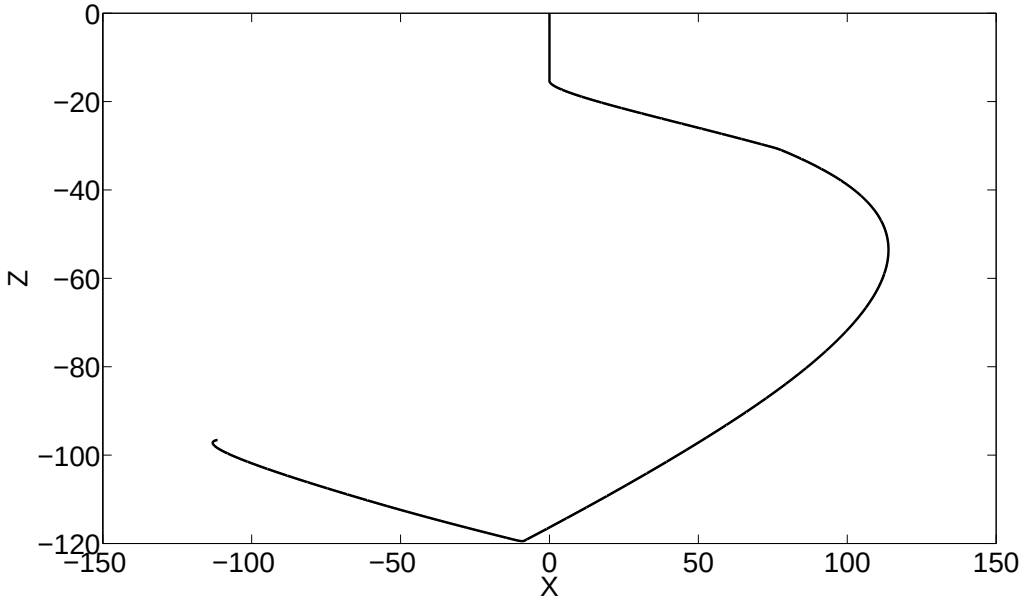

Figure 4.15: Falling with the Wind Scheme: $(x - z)$ Positions

The results in Figs 4.13, and 4.15 prove the possibility to control the motion of the AES. By controlling the angle of inclination of the windmill, (θ), the parameters that affect the dynamic motion of the system can be stabilized through controlling the velocity of the system in a specific direction. Furthermore, these results indicate the ability of the system to fly on, and follow a specific path which may be utilized to create a closed-path in the wind field. However, it can be observed that no significant lift is generated, and the system needs to be modified, and occupied with a lifting mechanism to maintain a closed-path. Consequently, the design of AES can be developed to incorporate the Powered-rotation mode of operation that provides the system with the ability to switch from autorotation flight to a powered flight to generate to required lift.

4.3 Energy Extraction Simulation Results

The performance of our proposed AES model during energy harvesting operation is also investigated through simulation. The $Dynamic\,\mu$ approach, described in section (3.3), is considered to conduct a set of simulation to compute the extracted power for a range of (Q_e) values. We first present the results of the simulation for ($Q_e = 0$) to be compared with the $Static\,\mu$ approach's results of the pure autorotation mode introduced in the previous section (4.2). Subsequently, the performance results of the system using different values of (Q_e) are presented.

4.3.1 Pure Autorotation Mode, $Q_e = 0$

A set of simulations to examine the performance of the system using the $Dynamic\,\mu$ approach is implemented. In these simulations, the braking torque (Q_e) is assumed to be $zero$ and the values of the angle (θ) are used similar to those considered for the schemes that are introduced in subsection (4.2.4).

We first implement the $Falling\,Against\,the\,Wind$ scheme in which the angle (θ) is changed to the values $(0, -4, 10^{\circ})$ sequentially. Figure 4.16 shows the results that compare the $(x - z)$ position of the system with those from Fig 4.13. We also run another simulation using the values of the angle (θ) that are utilized in $Falling\,with\,the\,Wind$ scheme. We first set (θ) to $zero$, then we change it to $(4, -8, 8^{\circ})$ sequentially. The result of this flying scenario combined with the result shown in Fig 4.15 , both are presented in Fig 4.17.

By comparing the $Dynamic\,\mu$ approach's results shown in Figs 4.13 and 4.17 with the $Static\,\mu$ approach's results, it can be observed that there is no significant change in the performance of the system. Therefore, the ability of using the $Dynamic\,\mu$ approach in the energy harvesting analysis is confirmed.

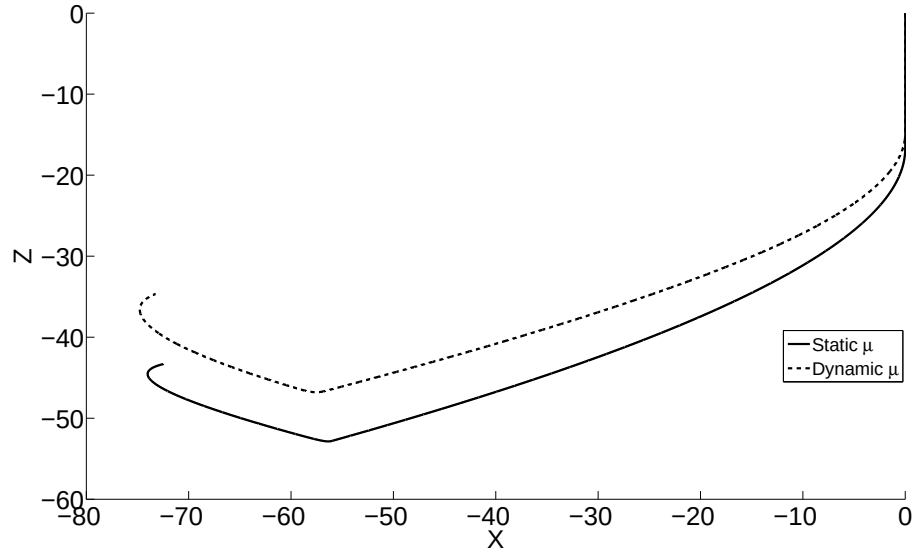

Figure 4.16: Falling Against the Wind Scheme: $Static$ and $Dynamic\,\mu$

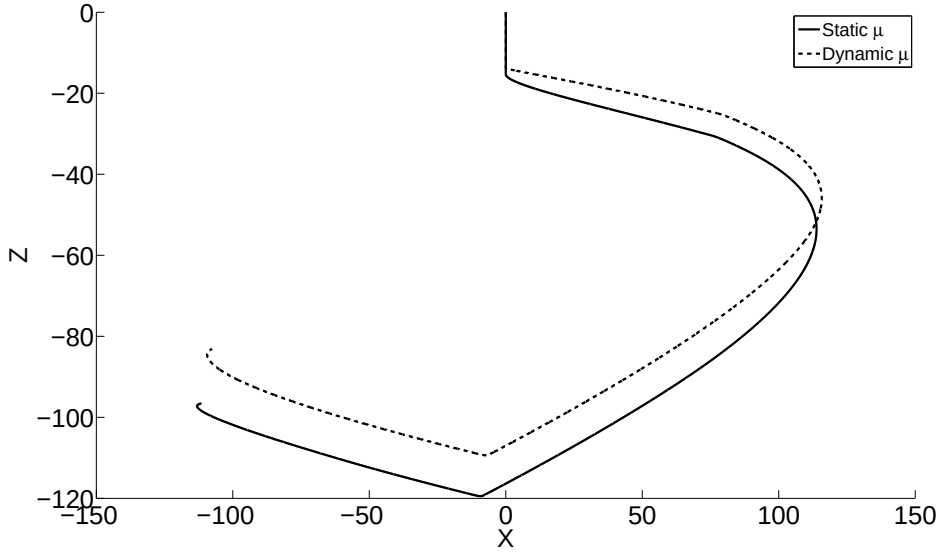

Figure 4.17: Falling with the Wind Scheme: $Static$ and $Dynamic\,\mu$

4.3.2 Energy Extraction Mode

In this subsection, the simulation tests are carried out to explore energy extraction process of AES for a range of (Q_e) values. The results are shown below. Figure 4.18 shows the flying path of the system for the $Falling\,Against\,the\,Wind$ scheme with different values of (Q_e), while the Fig. 4.19 shows the amount of the extracted power of each considered braking torque.

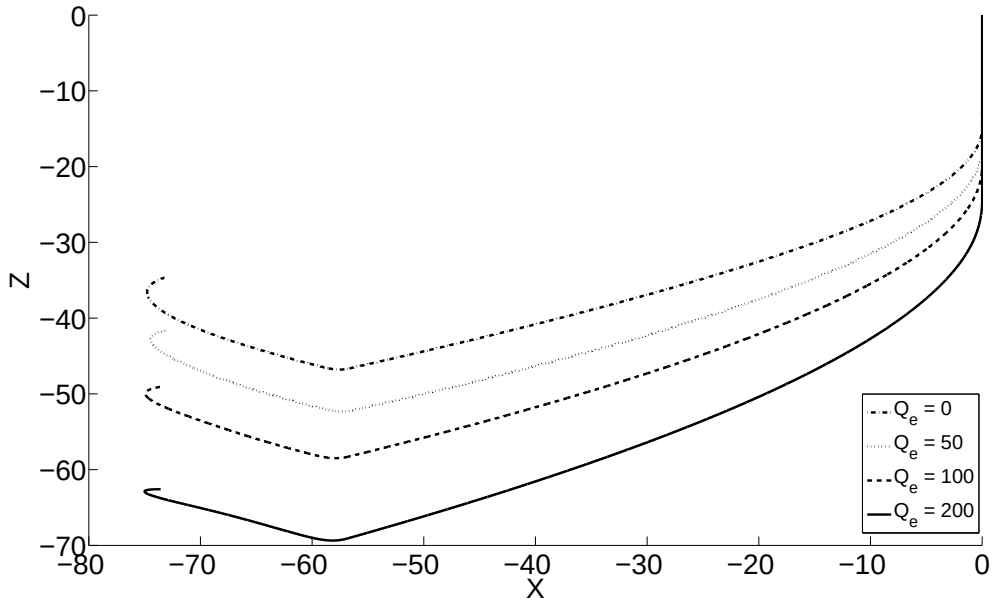

Figure 4.18: Falling Against the Wind Scheme, Various Values of Q_e

It can be observed from the Fig. 4.18 that AES performance is generally similar for all the selected values of (Q_e). However, we can infer from these results that the velocity of AES along the negative (Z) axis, increases with the increase of the value of (Q_e). This can be explained by the fact that raising the braking torque reduces the angular velocity (Ω) that affects the thrust force (T)

and decreases its amount. Consequently, the ability of the system to provide an opposite force to handle its weight is minimized. On the other hand, the results presented in Fig. 4.19 indicate that the higher the value of (Q_e), the higher the amount of the generated power that can be harvested. The power result show that AES can generate more than $800\,W$ of power with ($Q_e = 200$) and total weight of ($50\,Kg$).

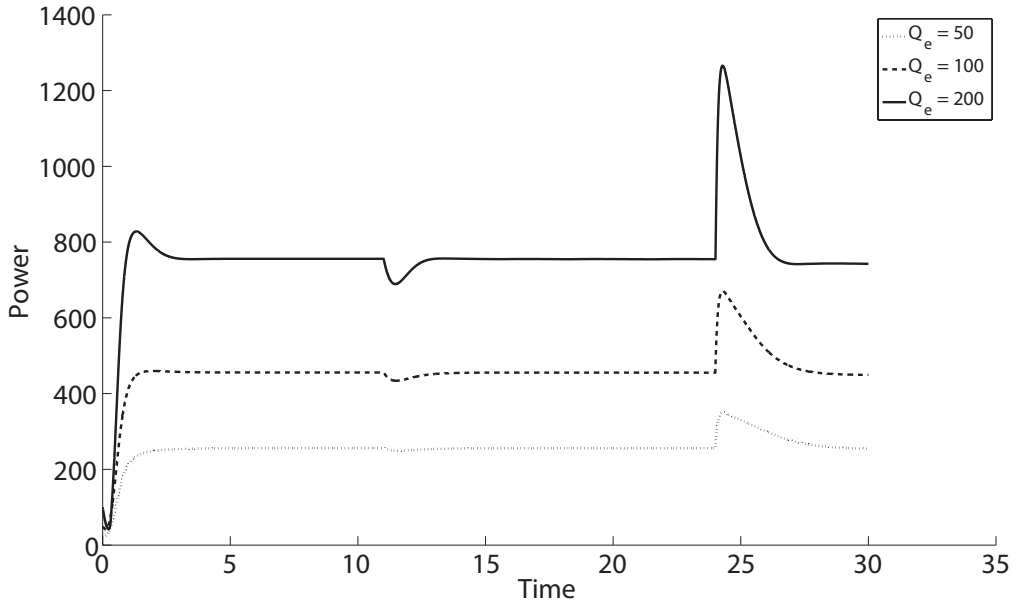

Figure 4.19: Falling Against the Wind Scheme,Power Results for Different Values of Q_e

Figures 4.18 and 4.21 present the flying path of the system and the amount of the extracted power for the $Falling\,with\,the\,Wind$ scheme with different values of (Q_e) respectively. Similar observations to those made from the performance of AES while falling against the wind can be presented for the $Falling\,with\,the\,Wind$ scheme. Generally, the behavior of the system remains the same for all the chosen values of (Q_e) but the velocity (V_z) increases due to the decrease of the angular velocity (Ω) and the thrust force (T). Furthermore, the extracted power is almost identical for the

both introduced schemes because of the similarity in their angular velocity (Ω).

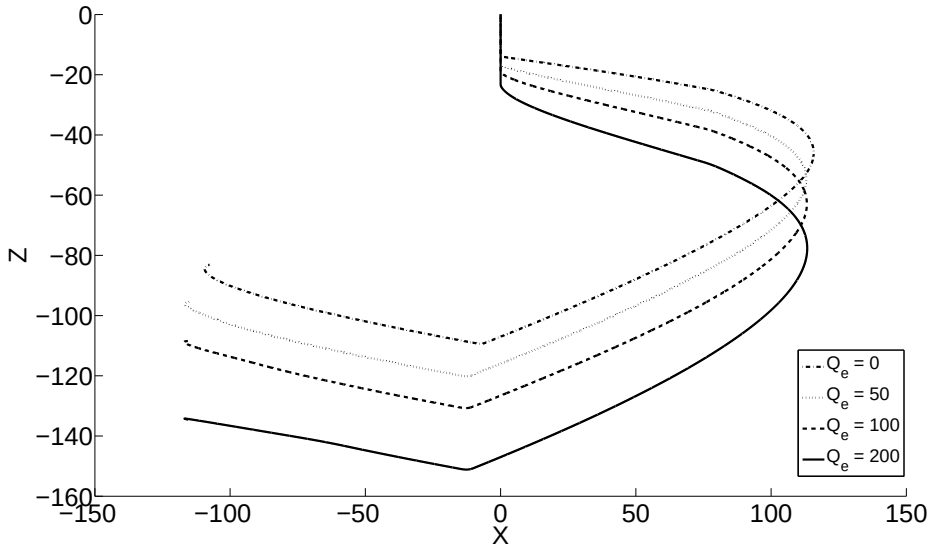

Figure 4.20: Falling with the Wind Scheme, Various Values of Q_e

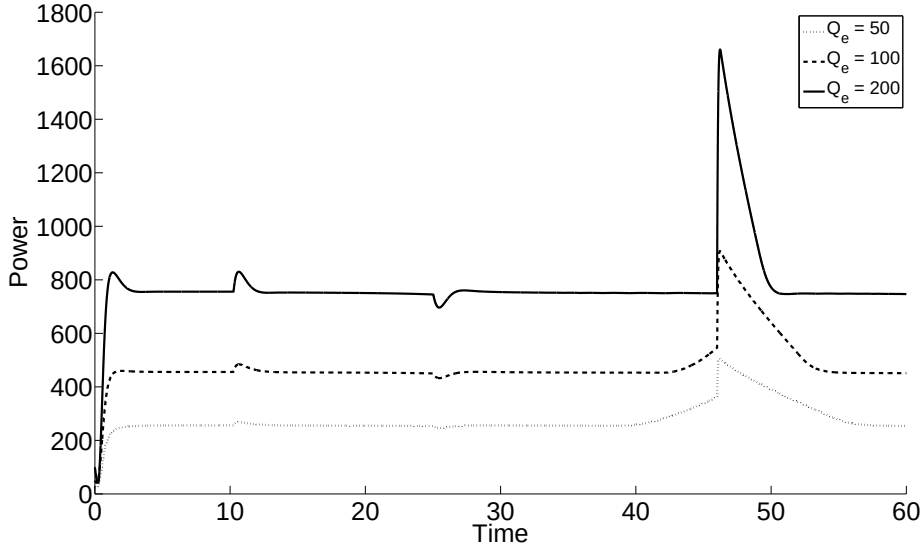

Figure 4.21: Falling with the Wind Scheme,Power Results for Different Values of Q_e

CHAPTER 5: CONCLUSION

In this thesis research, we considered the topic of harvesting wind energy from high altitudes or from strong wind field, and explored the possibility of utilizing the autorotation phenomenon for designing an Autorotation Energy System (AES) that can simultaneously fly and generate energy from high altitudes. We first studied and analyzed two existing airborne devices which are proposed for wind energy harvesting, the tethered airfoil, and the static autogyro. These studies revealed that untethered AES, that is agile and maneuverable, is preferred for energy harvesting. The aim of this research was to provide a preliminary dynamic analysis of AES. Hence, we proposed a simple dynamic model of a single autogyro, and developed a simulation platform to get a clearer picture about the dynamics of autorotation. This is in contrast with existing works on autorotation that exclusively focus on static autorotation with application to helicopter. Subsequently, we provided comprehensive results about the autogyro's rudimentary maneuvers. we extensively carried out simulations to evaluate the dynamic performance of AES and the impact of braking torque that is used to simulate the effect of energy harvesting. In practice, the rotor will be hosted inside a generator, and deriving actual force will result in a braking torque. We provided simulation results for different hovering scenarios by using different system masses, various values of the windmill angle of inclination with the horizon (θ), and variable range of the braking torque (Q_e). The simulation results indicated the possibility of utilizing the autorotation concept, and supported the potential viability of using AES to harvest energy from strong wind field. Meanwhile, the proposed AES can not remain inertially static in a wind field during the autorotation mode, and its stability was addressed to be a challenging issue.

An interesting finding is the ability of the system to fly with as well as against the direction of the wind, and this implied the possibility of controlling the motion of AES via controlling the angle of inclination (θ). Moreover, the results indicate the possibility of the system to generate

a closed-path (trajectory) in the wind field if a mechanism for powered-rotation is incorporated. Powered flight can be incorporated in the design of AES, since autogyro is a generalized rotorcraft. Consequently, a periodic trajectory can be achieved by switching between autorotation and powered-rotation modes such that over one period, a closed-path is maintained. Figure 5.1 shows two scenarios of a simplified $2D$ periodic trajectory.

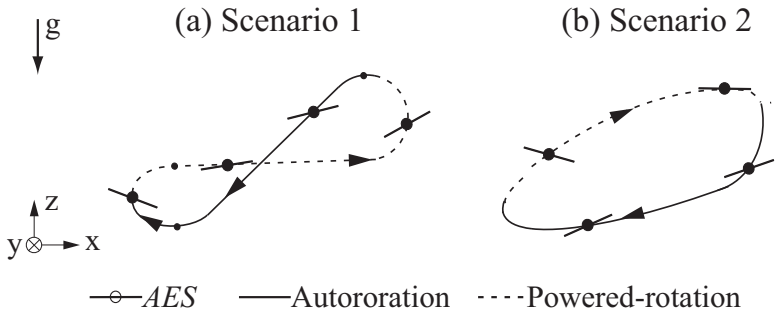

Figure 5.1: Two Periodic Trajectory Scenarios

The flying trajectory could be also a drifting trajectory from a starting point A to a destination B as shown in Fig 5.2.

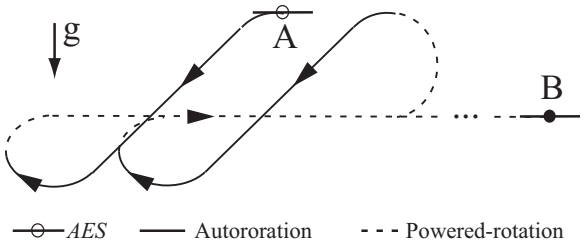

Figure 5.2: A Drifting Trajectory Scenario

While the results of this thesis provided an overall dynamic performance picture of AES in term of hovering and maneuvers, the proposed model needs to be more investigated in future research and studies to further validate the approach. This work can be developed to have more accurate model by relaxing some of the approximations and assumptions such as considering the affect of the longitudinal force (H), the lateral torque, etc. An important future research idea is to extend this work to consider the flapping of the windmill blades about the hinge at their roots, and derive new equations to define the dynamics of the flapping angle (ϖ). Another important future research topic is to find the energy- optimal path in wind fields by investigating the overall energy efficiency of trajectories through formulating optimization problems. Furthermore, the results of this thesis can be utilized in future research works to guide the choice of actuations and control approaches. From a control standpoint, this work can be extended by designing the required mechanism to control the angle (θ).

A multi-rotor based AES such as quadrotors is likely to be the final design due to their well demonstrated controllablility and maneuverability. Furthermore, this choice is driven by the vast literature on quadrotors that can be used as a base to build on. Hence, a quadrotors configuration having simple blade geometries and simple rotor actuation will be of interest in our future research instead of single rotors. Figure 5.3 shows the suggested quadrotors configuration.

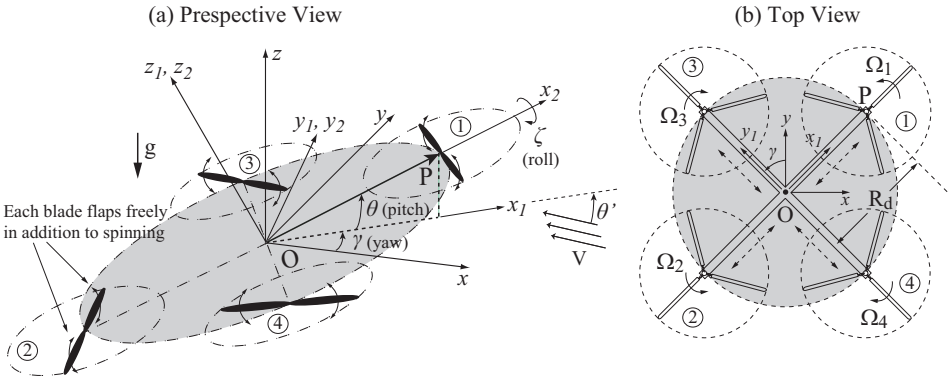

Figure 5.3: AES in a Quadrotor Configuration

In order to achieve in-flight energy harvesting capability and maneuverability, the configuration of the quadrotors requires designing a dynamic model of AES that can operate in dual modes, the autorotation and the powered-rotation modes. The latter mode will consume some of the produced energy during the autorotation mode to provide the system with the required lift to maintain a closed-path. Controlling the switching between the autorotation and powered flight modes will be another interesting problem to be investigated. Figure 5.4 shows the two modes of operations and illustrates the difference between their operating principles. Figure 5.4 (a) represents the Autorotation mode of operation while Fig 5.4 (b) shows the powered-rotation mode.

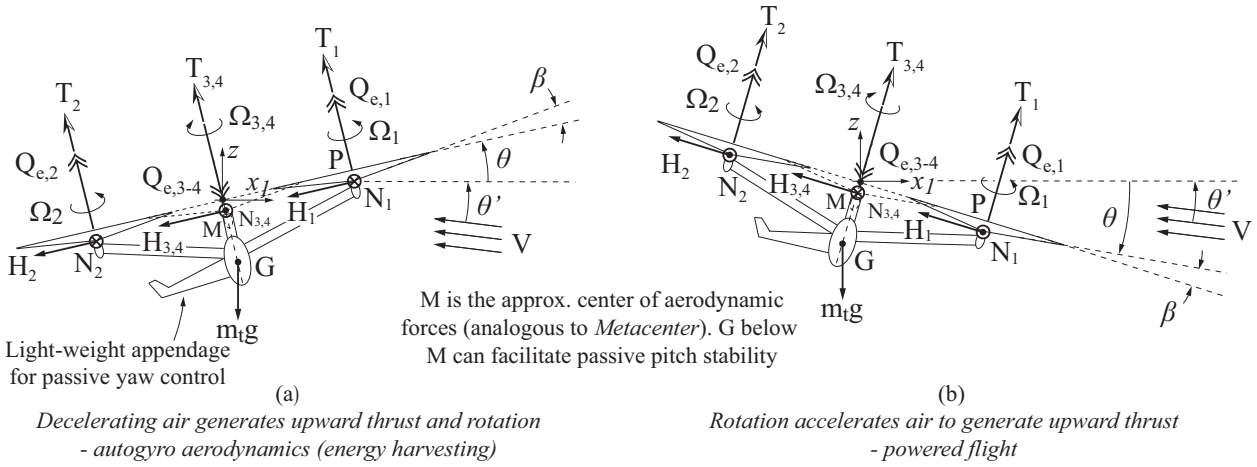

Figure 5.4: AES Quadrotor Operation Modes

Finally, this work can be extended in many other ways such as the design of tethered AES device, the stability analysis of AES, and potentially extending to study energy harvesting from water currents.

LIST OF REFERENCES

[AC09] C. L. Archer and K. Caldiera. Global assessment of high-altitude wind power. In *Energies*, volume 2, pages 307–319, 2009.

[AJ10] J. D. Anderson Jr. *Fundamentals of Aerodynamics*. McGraw-Hill, 2010.

[AJ11] J. D. Anderson Jr. *Introduction to Flight*. McGraw-Hill, 7th edition, 2011.

[CFIM06] M. Canale, L. Fagiano, M. Ippolito, and M. Milanese. Control of tethered airfoils for a new class of wind energy generator. *IEEE Conference on Decision and Control, San Diego, CA*, 2006.

[CFM09] M. Canale, L. Fagiano, and M. Milanese. Kitegen: A revolution in wind energy generation. *Energy*, 34:355–361, 2009.

[CFM10] M. Canale, L. Fagiano, and M. Milanese. High altitude wind energy generation using controlled power kites. *IEEE Transactions on Control Systems Technology*, 18 (2):279–293, 2010.

[CFMI07] M. Canale, L. Fagiano, M. Milanese, and M. Ippolito. Kitegen project: Control as key technology for a quantum leap in wind energy generators. *Proceedings of the American Control Conference, New York, NY*, pages 3522–3528, 2007.

[Cha03] B. H. Charnov. *From Autogyro to Gyroplane: The Amazing Survival of an Aviation Technology*. Praeger Publishers, 2003.

[DM+11] T. Das, R. Mukherjee, , R. Sridhar, and A. Hellum. Two dimensional modeling and simulation of a tethered airfoil system for harnessing wind energy. *ASME Dynamic Systems and Control Conference*, 2011.

[DVW06] I. Durre, R. S. Vose, and D. B. Wuertz. Overview of the integrated global radiosonde archive. *Journal of Climate*, 19(1):53–68, 2006.

[ESH+11] D. Elliot, M. Schwartz, S. Haymes, D. Heimiller, G. Scott, M. Brower, E. Hale, and B. Phelps. New wind energy resource potential estimates for the united states. Technical Report NREL Report No. PR-5500-50439, National Renewable Energy Laboratory, 2011.

[FH78] C. M. Fry and H. W. Hise. Driven high altitude power apparatus. *US Patent 4,084,102*, 1978.

[Fle79] C. A. J. Fletcher. On the rotary wing concept for jet stream electricity generation. In *Journal of Energy*, 1979.

[FR79] C. A. J. Fletcher and B. W. Roberts. Electricity generation from jet stream winds. *Journal of Energy*, 3:241–249, 1979.

[Gla26] H. Glauert. A general theory of the autogyro. Technical report, Aeronautical Research Council, 1926.

[GM52] A. Gessow and G. C. Myers. *Aerodynamics of the Helicopter*. Macmillan Company, 1952.

[GSH12] M. Garcia-Sanz and C. H. Houpis. *Wind Energy Systems: Control Engineering Design*. CRC Press, 2012.

[Hod09] B. K. Hodge. *Alternative Energy Systems and Applications*. John Wiley & Sons, Inc., 2009.

[Kli78] A. Kling. Wind driven power plant. *US Patent 4,073,516*, 1978.

[Lei00] J. G. Leishman. *Principles of Helicopter Aerodynamics*. Cambridge University Press, 2000.

[LW06] B. Lansdorp and P. Williams. The laddermill - innovative wind energy from high altitudes in holland and australia. *Windpower, Adelaide, Australia*, 2006.

[Man75] M. S. Manalis. Airborne windmills: Energy source for communication aerostats. In *AIAA Lighter Than Air Technology Conference*, 1975.

[Ock01] W.J. Ockels. Laddermill, a novel concept to exploit the energy in the airspace. *Aircraft Design*, 4(81-97), 2001.

[Phe] Gyrocopter vs helicopter. `http://www.phenix.aero/PHE-1210.html`.

[PM07] Pallav Purohit and Axel Michaelowa. Potential of wind power projects under the clean development mechanism in india. In *Carbon Balance and Management*, 2007.

[Pug84] P. F. Pugh. Wind generator kite system. *US Patent 4,486,669*, 1984.

[RD13] Sigitas Rimkus and Tuhin Das. An application of the autogyro theory to airborne wind energy extraction. In *ASME Dynamic Systems and Control Conference*, 2013.

[RR84] G. Riegler and W. Riedler. Tethered wind systems for the generation of electricity. *Journal of Solar Energy Enegineering*, 106:177–181, 1984.

[RSC+07] B. W. Roberts, D. H. Shepard, K. Caldiera, M. E. Cannon, D. G. Eccles, A. J. Grenier, and J. F. Freidin. Harnessing high-altitude wind power. In *IEEE Transactions on Energy Conversion*, volume 22, pages 136–144, 2007.

[Rye85] D. C. Rye. Longitudinal stability of a hovering tethered rotorcraft. *Journal of Guidance, Control and Dynamics*, 8(6):743–752, 1985.

[SN01] J. Seddon and S. Newman. *Basic Helicopter Aerodynamics*. AIAA, 2th ed. edition, 2001.

[Whe34] John B. Wheatley. An aerodynamic analysis of the autogiro rotor with a comparison between calculated and experimental results. 487, National Advisory Committee for Aeronautics, 1934.

[Whi09] F.M. White. *Fluid Mechanics*. McGraw-Hill, 7th ed. edition, 2009.

[WLO07] P. Willams, B. Lansdorp, and W. Ockels. Modeling and control of a kite on a variable length flexible inelastic tether. *AIAA Modeling and Simulation Technologies Conference and Exhibit*, 2007.

[WLO08a] P. Willams, B. Lansdorp, and W. Ockels. Optimal cross-wind towing and power generation with tethered kites. *AIAA Journal of Guidance, Control and Dynamics*, 31, 2008.

[WLO08b] P. Williams, B. Lansdorp, and W. J. Ockels. Nonlinear control and estimation of a tethered kite in changing wind conditions. In *AIAA Journal of Guidance, Control, and Dynamics*, 2008.